

Acid-sulfate weathering of synthetic Martian basalt: The acid fog model revisited

Nicholas J. Tosca, Scott M. McLennan, Donald H. Lindsley, and Martin A. A. Schoonen

Department of Geosciences, State University of New York, Stony Brook, New York, USA

Received 18 November 2003; revised 25 March 2004; accepted 5 April 2004; published 19 May 2004.

[1] The acid fog model has received considerable attention as a model of soil formation on Mars. Previous evaluations of this model have focused on experimental weathering of terrestrial basalt samples. However, these samples differ significantly from what now is thought to be typical of Martian basalt. The acid fog model is tested here using synthetic basaltic analogs derived from Mars Pathfinder soil and rock compositions. Reaction of synthetic basalt with various acidic solutions and subsequent evaporation has led to the formation of several putative secondary mineral phases. Many of these phases were not produced in prior experimental studies aimed at aqueous interactions on Mars. Of these alteration phases, Mg, Fe, Ca, and Al sulfates were identified. In addition, secondary ferric oxide phases formed via rapid Fe oxidation under relatively high pH levels buffered by basalt dissolution. Amorphous silica is a ubiquitous product in these experiments and has formed by precipitation from solution and by the dissolution of minerals and glasses leaving behind leached surface layers composed of residual silica. The secondary products formed in these experiments demonstrate the importance of primary mineralogy when testing models of aqueous interactions on Mars. New constraints are placed on both the reactivity of primary basalt and the secondary mineralogy present at the Martian surface.

INDEX TERMS:

1045 Geochemistry: Low-temperature geochemistry; 3630 Mineralogy and Petrology: Experimental mineralogy and petrology; 3672 Mineralogy and Petrology: Planetary mineralogy and petrology (5410); 5415 Planetology: Solid Surface Planets: Erosion and weathering; 5470 Planetology: Solid Surface Planets: Surface materials and properties; *KEYWORDS:* geochemistry, Mars, weathering, acid fog, sulfates, silica

Citation: Tosca, N. J., S. M. McLennan, D. H. Lindsley, and M. A. A. Schoonen (2004), Acid-sulfate weathering of synthetic Martian basalt: The acid fog model revisited, *J. Geophys. Res.*, 109, E05003, doi:10.1029/2003JE002218.

1. Introduction

[2] The chemical and mineralogical nature of the sedimentary material mantling the Martian surface holds information of past climatic conditions on Mars. The possibility of liquid water present on the surface of Mars at one time during its history suggests that the Martian regolith may have been subject to a variety of chemical processes leading to its present state. This has led to much effort in the characterization of the Martian surface using spectroscopic techniques by orbiters and Earth-based telescopes [Bandfield, 2002; Bell, 1996; Soderblom, 1992]. In addition, chemical data from the Martian surface obtained by landers, as well as data from Martian meteorites, have shed light on the history of water on the red planet [Bell *et al.*, 2000; Bridges and Grady, 1999; Bridges *et al.*, 2001; Toulmin *et al.*, 1977]. As a result, some models have been proposed to provide formation mechanisms for individual secondary minerals or for the Martian soil as a whole.

[3] Some models have been formulated by using terrestrial weathering environments as Martian analogs and, in few instances, have been based on experimental investiga-

tions involving the chemical alteration of terrestrial analog basalt [Baker *et al.*, 2000; Banin *et al.*, 1997; Golden *et al.*, 1993; Morris *et al.*, 1990, 2000a, 2000b]. However, most terrestrial basalt differs significantly in bulk chemistry and consequently, mineralogy when compared to suggested Martian basalt compositions. Therefore the primary goal of this study is to demonstrate the dependence on primary mineralogy (among several other factors) in chemical weathering studies applied to the surface of Mars using analog basalt synthesized in the laboratory. This is accomplished by using what is referred to as the “acid fog” model [Banin *et al.*, 1997; Settle, 1979] as an example of the importance primary composition can have in the production of secondary alteration phases. Testing this model provides constraints on the fundamental geochemical processes common to several alteration scenarios and their importance to the surface of Mars.

[4] The acid fog model has become widely accepted as a viable mechanism for Martian soil formation. The primary goal of the model is to explain the lack of well crystalline material in the uppermost portion of the Martian sediment, a reservoir sampled by the Pathfinder and Viking missions [Banin, 1996; Banin *et al.*, 1997]. The mechanism at work in this model can be summarized as the interaction of the Martian basaltic crust with volcanically derived acidic

volatiles. This interaction may include volcanic aerosol-basalt interactions or acidic fluid-basalt interactions resulting from the mixing of volatiles with water vapor or small amounts of transient water already on the surface of Mars. The acidic fluid interactions with basalt result in mineral/glass dissolution and occur in low fluid-to-rock ratios. Upon evaporation of the fluid after relatively short reaction time-scales (the model assumes that aqueous fluids at the surface are by nature transient), sulfate and possibly chloride salt minerals are formed as well as amorphous, or poorly crystalline silicate and ferric iron oxide phases.

[5] *Banin et al.* [1997] first tested the acid fog model experimentally by acidifying volcanic tephra from Mauna Kea, Hawaii. The fluid-to-rock ratio was maintained at 1:1 throughout the experiments. Upon evaporation of the fluid after a total of 14–15 days, *Banin et al.* [1997] detected aluminum and calcium sulfate salts (alunogen and gypsum, respectively) by X-ray diffraction. Unfortunately, the present limited data constraining secondary mineralogy of the Martian soil do not suggest that either of these phases is likely to be present, at least at the Viking and Pathfinder landing sites. However, performing weathering experiments on synthetic analog Martian basalts provides a more robust test of this model. In addition, the primary composition and crystallinity of the basalt, as well as solution concentrations, are all varied in this study. Furthermore, a broad spectrum of analytical tools is employed in order to characterize the poorly crystalline secondary alteration minerals, the formation of which was proposed in the original model.

[6] Basalt alteration is a complex process and can result in the formation of several secondary mineral phases. Accordingly, a wide variety of such phases are suggested to be important to the Martian surface. These phases include: sulfates and chlorides [e.g., *Banin et al.*, 1997; *Bishop and Murad*, 1996; *Clark and Van Hart*, 1981; *Morris et al.*, 1996], hydroxylated/hydrated minerals [e.g., *Gooding*, 1992], a variety of secondary iron oxides [e.g., *Bell*, 1996; *Bell et al.*, 1990, 2000; *Christensen et al.*, 2000], clay minerals [e.g., *Banin and Margulies*, 1983; *Bell*, 1996; *Bishop et al.*, 1993; *Gooding and Keil*, 1978], carbonates [e.g., *Morse and Marion*, 1999], zeolites [e.g., *Bish et al.*, 2003; *Gibson et al.*, 2003], amorphous silica [e.g., *McLennan*, 2003], and an “amorphous mineraloid” referred to as palagonite [*Allen et al.*, 1981; *Morris et al.*, 1990, 2003], which, in some cases, is actually an assemblage of poorly crystalline minerals. The formation and stability of these phases can be complicated and are dependent on several factors. However, an evaluation of aqueous processes on Mars beginning with initial chemical interactions with relevant Martian basaltic analogs may begin to place constraints on the importance of such phases in the context of the acid fog model.

2. Data Manipulation and Methods

2.1. Derivation of Analog Compositions

[7] The basaltic analog compositions used in this study are derived from the average recalibrated Pathfinder Alpha Proton X-ray Spectrometer (APXS) data published from *Economou* [2001] and *Wänke et al.* [2001]. Data for Na₂O were taken only from *Economou* [2001], who used data from alpha particle analytical mode of the APXS, which

yield more reliable Na₂O data than the X-ray mode (see *Foley et al.* [2003] for further discussion).

[8] Two important characteristics of the APXS data obtained from the Pathfinder mission are the elevated SO₃ and Cl levels present in the soil samples, widely interpreted to be chemical measures of alteration. The data for almost all of the major elements present in Pathfinder soils and rocks, as well as Viking lander soils, correlate negatively (with varying degrees of uniformity) with increasing SO₃ content [*Rieder et al.*, 1997]. The only exceptions to this trend are Fe and Mg, which correlate positively with increasing SO₃ content. Some workers suggest that these data represent a simple two-component mixing relationship between rock and soil components [e.g., *Rieder et al.*, 1997; *Bell et al.*, 2000; *McSween and Keil*, 2000]. As an attempt to account for the layer of soil that appears to have adhered to rocks at the Pathfinder site, some authors have suggested a “soil-free” rock composition [e.g., *McSween et al.*, 1999; *Minitti and Rutherford*, 1999; *Rieder et al.*, 1997]. These compositions were derived by the extrapolation of the observed elemental trends between the Pathfinder rock and soil data to zero (or low, e.g., 0.3 wt% SO₃) sulfur content.

[9] A slightly different approach is adopted here to estimate the low-S Pathfinder rock composition (termed PFR). The lowest sulfur Pathfinder rock (A17) is assumed to be a mixture of some primary rock and the average of the two highest sulfur soils (A4 and A10). We calculated the A17 rock analysis to contain 21% of the A4/A10 soil mixture and then determined individual major element abundances by linear unmixing to 0.0 wt% SO₃. The calculated composition was then normalized to 100% on a Cl-free basis. The resulting composition (PFR) is shown in Table 1. This approach was adopted because *McLennan* [2000] noted that linear regressions of element abundances versus S content did not correspond to calculated mixing lines. In any case, the resulting composition listed in Table 1 agrees well with the two most recent estimates of “soil-free” rock compositions, reported by *Foley et al.* [2003] and *Wänke et al.* [2001], in all major elements with the exception of Al₂O₃, and CaO. These elements display scatter among Pathfinder rock and soil analyses when plotted against SO₃, which causes differences in the slopes of trend lines depending on which analyses are included in the regression calculations.

[10] Two-component mixing between Pathfinder rocks and soils has most likely been complicated by a variety of possible sedimentary processes acting on the surface of Mars [*McLennan*, 2000]. As a result, the geological meaning of “soil-free” rock is unclear. Regardless of the exact calculation, the “soil-free” rock composition (e.g., PFR) is likely to be a better estimate of typical Martian basalts than are most terrestrial analogs.

[11] Another characteristic of the APXS data from the Pathfinder site is the overall broad similarity to the Viking lander soil analyses, the farthest of which is 6900 km from the Pathfinder landing site. This chemical similarity, coupled with evidence of persistent aeolian activity such as planet-wide dust storms as well as the fine grained nature of the Martian surface layer suggest that primary and secondary products formed from the exposed crust have been well homogenized. If this is the case, then the existing soil data obtained from Mars may be representative of an average upper-most crustal composition (excluding S and Cl)

Table 1. Synthetic Analog Bulk Composition and Accuracy

	PFR Target log $f_{O_2} = -10$	PFR Average (Synthesized Comp.) ^a	PFR Accuracy (Synthesized/Target)	PFS Target log $f_{O_2} = -7.5$	PFS Average ^b (Synthesized Comp.)	PFS Accuracy (Synthesized/Target)	M. Kea Tephra ^c 91–16
SiO ₂	57.14	57.87	1.01	48.42	48.68	1.01	48.50
TiO ₂	0.52	0.51	0.97	1.17	1.16	1.00	3.50
Al ₂ O ₃	10.34	10.36	1.00	10.29	10.29	1.00	19.60
FeO _T	14.02	13.73	0.98	19.10	19.23	1.01	12.60
MnO	0.44	0.46	1.05	0.49	0.49	0.99	0.20
MgO	2.60	2.47	0.95	8.00	7.66	0.96	4.20
CaO	8.70	8.68	1.00	7.15	7.07	0.99	6.40
Na ₂ O	4.60	4.28	0.93	3.55	3.56	1.00	3.50
K ₂ O	1.09	1.11	1.02	0.65	0.67	1.02	1.10
P ₂ O ₅	0.55	0.54	0.97	1.18	1.19	1.01	0.60
Total	100.00	100.00	—	100.00	100.00	—	100.20

^aAverage of 24 electron microprobe analyses, normalized to 100.00 wt%.^bAverage of 25 electron microprobe analyses, normalized to 100.00 wt%.^cMauna Kea tephra sample 91–16, used as an analog by *Banin et al.* [1997]. Recalculated volatile-free (4.8% LOI reported).

[McLennan, 2001; McSween and Kiel, 2000]. Such a composition is also suitable to test as a basaltic analog in this study. The Pathfinder soil composition (PFS) used here is simply an average of Pathfinder soil data (from above sources) recalculated on a S- and Cl-free basis (Table 1). It should be noted that the resulting Fe and Mg abundances have been slightly reduced from the initial calculation in order to lower the liquidus of the composition and stay within the operational temperature range capable of Pt-wound furnaces (described in section 2.2) during syntheses.

2.2. Experimental Methods

2.2.1. Basalt Analog Synthesis

[12] After the bulk chemical composition is derived, that composition is calculated into an equivalent mixture of 11 oxide and silicate components that can be physically mixed to represent the composition. The individual components were accurately weighed and transferred to an automatic agate mortar/pestle grinder where they were ground and mixed under ethanol for a total of 3 to 3.5 hours. The Fe³⁺/Fe²⁺ ratio present in the mixtures controls the redox conditions during melting experiments, and therefore, by varying this ratio, one can attain desired oxygen fugacities. Target oxygen fugacities (listed in Table 1) were chosen using the temperature- f_{O_2} relationship for basaltic shergottites from data calculated by *Herd et al.* [2001].

[13] After the mixture is ground, it is dried thoroughly and packed and enclosed in an Au₈₀Pd₂₀ alloy tube approximately 2.5 cm in length and 0.5 cm in diameter. The Au₈₀Pd₂₀ tube is placed in a silica glass tube, which is already sealed at one end and is then drawn out into a thin capillary at the open end. The silica tube is evacuated while drying at 800°C for a period of 30 minutes. During this process, a small piece of Fe metal is placed above the capillary (a geometry chosen such that the Fe metal is at approximately 600°C) to promote the reduction of any volatiles left in the sample tube, or possibly diffusing back into the tube from the vacuum, which may rapidly oxidize the sample. The capillary is then melted and severed with an oxygen/natural gas torch under vacuum, creating a sealed tube assembly at a pressure of “0 kbar”.

[14] During the melting experiments, the silica tube assembly is suspended from two electrodes by a thin Pt metal wire in a vertical open-ended Pt₉₀Rh₁₀-wound furnace, where the mixture is slowly heated above its liquidus.

A current is then passed through the electrode holder in the furnace, melting the Pt wire, and allowing the silica tube to drop through the bottom of the furnace into a beaker of cold water to immediately quench the liquid, forming basaltic glass. The temperature of the furnace may also be programmed to follow a stepwise cooling path allowing the formation of crystalline basalt. This synthesis process yields, at the most, approximately 400 mg of basaltic material per 2.5 cm length of tubing (a maximum length, due to vertical temperature gradients within the furnace). To ensure the same synthesis conditions for all basalt used for a given aqueous batch experiment, up to three capsules can be reacted together in one furnace under identical conditions.

[15] Lastly, it is important to make note of steps taken to overcome two main complications of basalt synthesis. The first complication is that the samples lose Fe to the walls of the Au₈₀Pd₂₀ tubing during synthesis. Experimental results have shown that Fe loss in most systems used in this study is equal to approximately seven relative percent Fe^o by weight and is compensated for by adding excess Fe^o to oxide mixtures. The second complication results from the slow kinetics of plagioclase crystallization in synthetic systems, where two approaches were taken to aid its nucleation. The PFR composition, with a calculated liquidus of 1123°C, was synthesized with approximately 0.5 wt% plagioclase seed crystals. The resulting basalt was then used as a seed material for successive experiments, ensuring no significant effect on the bulk composition. For the PFS composition (calculated liquidus of 1246°C), adding the seed crystal did not result in plagioclase crystallization, most likely an effect of high-T melting conditions completely melting the seed crystals. Therefore another approach was used which involved subsolidus equilibration of the oxide mixture prior to synthesis at approximately 950°C for a period of 10 days. This process is believed to react CaSiO₃, Al₂O₃ and SiO₂ grains (from primary oxide components), which may form small amounts of anorthite in the oxide mixture, serving as a plagioclase seed stable up to higher temperature conditions. Upon synthesis of the pre-treated oxide mixture in the Pt-wound furnace, plagioclase was crystallized.

2.2.2. Aqueous Batch Experiments

[16] After synthesis, the basalt/glass is extracted from the Au₈₀Pd₂₀ tube and then crushed and sieved to a particle size to between 710 and 63 μ m (coarse to very fine sand). After

Table 2. Acid Mixtures Used in Alteration Experiments

Acid Mixture	H ₂ SO ₄ , mol/L	HCl, mol/L
A	1.0×10^0	2.5×10^{-1}
B	1.0×10^{-1}	2.5×10^{-2}
C	1.0×10^{-2}	2.5×10^{-3}
D	1.0×10^{-3}	2.5×10^{-4}
E	1.0×10^{-4}	2.5×10^{-5}

sieving, the basalt is ultrasonically rinsed several times with acetone to extract ultra-fine particles, which may adhere to larger basalt grains. The rinsed basaltic sample is then dried overnight at 120°C to remove residual acetone as well as trace amounts of water.

[17] When cooled, the basalt product is divided into five aliquots ranging from 200 to 300 mg each and added to mixtures of sulfuric and hydrochloric acids with varying concentrations. The acid mixtures are prepared using deionized water and reagent grade acids. The S:Cl molar ratio in each mixture is equal to 4, approximately the value observed in Pathfinder soils. The concentrations of the mixtures range from 1M H₂SO₄/0.25M HCl to 100 μ M H₂SO₄/25 μ M HCl, each decreasing in concentration by a factor of 10 (designated A-E in Table 2). The fluid-rock mixture is then enclosed in Savillex™ Teflon® beakers kept at 25.0 \pm 0.1°C in a water bath and allowed to react for a period of 14 days, periodically being opened to retain equilibration with the atmosphere. After the 14-day reaction period, the fluid in the beakers is evaporated carefully for two days at 45–55°C to prevent any volatilization of H₂SO₄ or HCl [Banin *et al.*, 1997]. When the evaporation process is complete, the solids are rinsed with anhydrous ethanol in a filter apparatus using a 0.45 μ m nitrocellulose filter and air dried to evaporate any remaining ethanol.

2.3. Analytical Methods

[18] Chemical analyses of pre-reacted synthetic samples were performed using a Cameca Camebax Micro electron microprobe equipped with four wavelength dispersive spectrometers as well as a Kevex Analyst 8000 energy dispersive detector. An accelerating voltage of 15 kV and a nominal beam current of 10 nA were used during all analyses. Analyses were conducted on thin sections of samples as well as on polished grains. Spot analyses on the samples ranged from a 10.30 μ m to a 1.08 μ m square raster depending on the size of the crystals analyzed. Analyses on Na bearing phases used the largest possible raster size to minimize Na volatilization.

[19] The mineralogy of the basalt was initially characterized by X-ray diffraction (XRD) with a Scintag PAD X diffractometer using Cu K α_1 radiation at 40 kV and 25 mA. Data were collected between 10 and 70 degrees 2 θ , with scan steps ranging from 0.02 to 0.05 degrees 2 θ .

[20] Ex situ aqueous analysis was performed on all experiments. The experiments were sampled over the course of the 14-day period for analysis by atomic emission spectroscopy so that the total fluid removed did not exceed 4% of the initial volume. During sampling, small amounts of fluid (approx. 0.02 g) were periodically extracted from the batch experiments and diluted to approximately 1 g with deionized water. The samples were mixed and then filtered through 0.20 μ m nylon syringe filters. Dilute hydrofluoric acid was added to all samples to ensure that any silica

present was kept in solution. The analyses were performed using a Beckman Spectraspan SSVB direct current plasma atomic emission spectrophotometer (DCP-AES), which gives total aqueous (with detection limits in μ mol/L listed in parentheses) Na (0.13), Mg (0.01), Al (0.07), Si (0.36), P (2.91), K (0.51), Ca (0.02), Ti (0.04), Mn (0.04), and Fe (0.09) concentrations. Analyses below detection limits are not included in data accompanying this study.

[21] Because of Na and K contamination from electrolyte solutions used in various pH electrodes, pH was not measured directly in solution. However, with a complete solution analysis and the assumption that the total S and Cl present in the fluids did not change, pH values were calculated by charge balance from speciation calculations using the geochemical modeling program, The Geochemist's Workbench® [Bethke, 2002]. It should be noted that precipitation of sulfate or chloride phases before the evaporation stage will significantly change the pH and calculated pH values will not reflect this, as no sulfate or chloride analyses were made during the experiments.

[22] At the conclusion of the batch experiments, the residual solids were characterized by XRD (described above). Analysis and peak matching of X-ray diffraction patterns of altered basalts was done using the program Crystallographica Search-Match®, which is an iterative phase identification program optimized for multiphase powder diffraction patterns. The multiphase patterns were matched against the Powder Diffraction File (PDF) (with restrictions on phase chemistry) and the phases with best fits were “extracted” from the pattern and searches were done on the resulting residual pattern. Conventional XRD analysis cannot detect the presence of smaller amounts of minerals, and therefore other techniques were used to identify these phases.

[23] Morphological and chemical information of secondary phases was obtained using a LEO 1550 SFEG scanning electron microscope (SEM) equipped with an EDAX energy dispersive X-ray spectrometer (EDS), which is capable of analyzing elements heavier than, and including C. Analyses were performed using an accelerating voltage of 15 kV and a 30 μ m aperture. The EDS system is also capable of quantitative elemental analysis, but only if the surface of the specimen is relatively flat. Most of the energy dispersive analyses discussed here are semi-quantitative because most analyses were performed on specimens with variable surface angles. However, the peak analysis software is capable of stoichiometric comparison between elements present in the spectra and, in most cases, can constrain the stoichiometry of the phase.

3. Results

3.1. Basalt Analog Synthesis: Results and Observations

[24] Electron microprobe analyses of synthesized basalts show that for both compositions used, the abundance of any given major oxide analyzed when compared to the target composition does not deviate by more than 7 relative percent (Table 1). Most of the major oxides in the two compositions differ by less than 2 relative percent, which is within the error associated with the electron microprobe analyses. The modal mineralogy of the crystalline basalts synthesized from both compositions is calculated by least

Table 3. Modal Mineralogy and Mineral Chemistry of Basaltic Analogs

PFR Basalt ^a		PFS Basalt ^a		Mauna Kea Tephra 91–16 ^b	
Olivine	0.0%	Olivine ($\text{Fe}_{0.65}\text{Fa}_{0.35}$)	16.6%	Olivine (Comp. not given)	Minor amount
High-Ca pyroxene ($\text{Wo}_{42}\text{En}_{30}\text{Fs}_{29}$)	31.4%	High-Ca pyroxene ($\text{Wo}_{37}\text{En}_{36}\text{Fs}_{27}$)	22.3%	High-Ca pyroxene	Not detected
Feldspar ($\text{Ab}_{73}\text{An}_{17}\text{Or}_{10}$)	60.1%	Feldspar ($\text{Ab}_{57}\text{An}_{41}\text{Or}_{02}$)	29.6%	Feldspar ($\text{Ab}_{70}\text{An}_{30}$)	Dominant phase
Fe-Ti oxides ($\text{Mt}_{89}\text{Usp}_{11}$)	3.3%	Fe-Ti oxides ($\text{Mt}_{69}\text{Usp}_{31}$)	10.5%	Fe-Ti oxides (Ti-rich magnetite)	Minor amount
Interstitial glass	5.2%	Interstitial glass	21.0%	Interstitial glass	–

^aModal abundances determined by least squares analysis of electron microprobe data.

^bMauna Kea tephra sample 91–16, used as an analog by *Banin et al.* [1997].

squares regression of electron microprobe results from individual mineral phases, interstitial glass and parent glass analyses. Petrographic analysis of thin sections allowed confirmation of the calculated modal abundances. The modal abundances of minerals present in crystalline basalts are close to those predicted using the thermodynamic modeling program MELTS [*Ghiorso and Sack*, 1995], indicating that the synthesized material was close to equilibration. Table 3 lists the modal mineralogy of PFR and PFS basalts as well as mineral compositions.

[25] Electron microprobe analyses on thin sections also allowed for determination of chemical heterogeneities in basaltic glasses. Several point analyses were conducted on each thin section to evaluate chemical gradients of the glass within the capsule. The composition of the glass from analysis to analysis showed that there were minimal chemical gradients which indicates that on a micron scale, the glasses were homogeneous and therefore close to full equilibration.

[26] For some crystalline basalts with coexisting Fe-Ti oxides, pyroxenes and either olivine or a silica phase, the QUIF program [*Andersen et al.*, 1993] was used to calculate the oxygen fugacity conditions during synthesis. For basalts with Fe-Ti oxides, pyroxenes, but no olivine or a silica phase, QUIF was used to calculate a range of possible oxygen fugacities present during synthesis. Calculated oxygen fugacity values do not deviate more than one log unit from the target in any synthesized basalt. The QUIF program was also used to calculate mineral formulae and site occupancy in pyroxenes. The parameters and methods inherent in the QUIF program for determining mineral formulae are described by *Andersen et al.* [1993] and references therein.

[27] When compared to the terrestrial basaltic analog used by *Banin et al.* [1997], the chemistry and mineralogy of the synthesized analogs are significantly different. Several notable differences in bulk composition can be seen in Table 1. The largest differences are in the most abundant elements such as Si, Al, Fe and Mg. The PFR and PFS analog compositions vary in bulk composition when compared to each other while still remaining unique when compared to most terrestrial basalts. The most important differences between the analogs include Si, Fe and Mg content.

[28] The large differences in bulk chemistry have a distinct effect on basaltic glass structure as well. *Poraj-Kosic* [1977] describes glasses as inorganic polymers with polymerized network-forming tetrahedral elements (such

as Si, Al, Fe^{3+}) cross-linked by ionically bonded network-modifying elements. These network-modifier elements satisfy the charge created by nonbridging oxygens of the aluminosilicate framework. The structure of glasses may change significantly depending on the proportions of network-forming or network-modifying elements present. With increasing proportions of network-modifying elements, there is an increase in nonbridging oxygens, which means that the overall silicate network is depolymerized which leads to an increase in structural disordering [*Bouska*, 1993; *Poraj-Kosic*, 1977]. As discussed below, this is important to basaltic glass weathering processes.

[29] Varying the bulk chemistry also affects the modal mineralogy of the basalts (Table 3). For example, *Banin et al.* [1997] reported the Mauna Kea tephra used in their experiments to be dominated by plagioclase with minor amounts of olivine and Fe-Ti oxides. The synthetic analogs include pyroxene, which is not observed in the Mauna Kea sample and lesser amounts of plagioclase. The importance of olivine weathering was evaluated in these experiments, because the PFS basalt contains approximately 17%, whereas the PFR basalt contains none.

[30] All of the minerals present in the synthesized basalts used in this study have been proposed to be important and likely primary mineral phases of Martian basalts. For example, low-Ca and high-Ca pyroxenes have been identified spectroscopically on Mars by several workers and are abundant in low-albedo Type 1 regions [e.g., *Mustard et al.*, 1993; *Mustard and Sunshine*, 1995; *Singer et al.*, 1979]. Also, pyroxenes were interpreted to be present in some regions in amounts as high as 25% [*Bandfield et al.*, 2000]. Olivine has also been identified in several locations on Mars with specific locations on the Martian surface with interpreted abundances up to 30% [*Hoefen et al.*, 2003]. In light of this and other evidence constraining primary basaltic mineralogy on Mars, ferromagnesian silicate minerals are important to include in the context of this model and when evaluating other models of Martian soil formation.

3.2. Aqueous Batch Experiments: Results and Observations

[31] In this section, the results of four major groups of experiments are discussed: PFR basalt, PFS basalt, PFR glass and PFS glass. Each section discusses two main points: controls on fluid chemistry and resulting secondary alteration phases. Full solution analyses for each experiment conducted are included in Appendix A (Figures A1–A8). In addition, a summary of the secondary alteration products

Table 4. Secondary Alteration Products Identified in This Study

	PFR Basalt					PFS Basalt					PFR Glass					PFS Glass				
	A	B	C	D	E	A	B	C	D	E	A	B	C	D	E	A	B	C	D	E
Hexahydrite ($\text{MgSO}_4 \cdot 6\text{H}_2\text{O}$)	–	–	–	–	–	X	X	–	–	–	–	–	–	–	–	X	–	–	–	–
$\text{MgSO}_4 \cdot \text{nH}_2\text{O}$	–	–	–	–	–	X	X	–	–	–	–	–	–	–	–	–	X	–	–	–
Rhombochalcite ($(\text{H}_5\text{O}_2)^+\text{Fe}^{3+}(\text{SO}_4)_2 \cdot 2\text{H}_2\text{O}$)	X	–	–	–	–	–	–	–	–	–	–	–	–	–	–	–	–	–	–	–
Melanterite ($\text{Fe}^{2+}\text{SO}_4 \cdot 7\text{H}_2\text{O}$)	–	–	–	–	–	–	–	–	–	–	–	–	–	–	–	–	X	–	–	–
$\text{FeSO}_4 \cdot \text{nH}_2\text{O}$	–	–	X	–	–	X	X	–	–	–	–	–	–	–	–	X	–	X	–	–
Hydroxylated Fe sulfate	X	X	–	–	–	–	–	–	–	–	–	–	–	–	–	–	–	–	–	–
Anhydrite (CaSO_4)	X	–	–	–	–	–	–	–	–	–	–	–	–	–	–	X	–	–	–	–
Gypsum ($\text{CaSO}_4 \cdot 2\text{H}_2\text{O}$)	X	X	X	X	–	X	X	X	X	–	X	X	–	–	–	X	X	X	X	–
Alunogen ($\text{Al}_2(\text{SO}_4)_3 \cdot 17\text{H}_2\text{O}$)	–	–	–	–	–	–	–	–	–	–	–	–	–	–	–	X	X	–	–	–
Tamarugite ($\text{NaAl}(\text{SO}_4)_2 \cdot 6\text{H}_2\text{O}$)	–	–	–	–	–	–	–	–	–	–	–	–	–	–	–	X	–	–	–	–
Na-sulfate	–	–	–	–	–	–	–	–	–	–	–	–	–	–	–	–	–	–	–	X
Misc. sulfate cement	–	–	–	–	–	–	–	–	–	–	X	X	X	–	–	–	–	–	–	–
Halite (NaCl)	–	–	–	–	–	–	–	–	–	–	–	–	–	–	X	–	–	–	–	–
Fe phosphate	–	–	–	–	–	–	X	X	X	–	–	–	–	–	–	–	–	–	–	–
Fe oxide (globular)	–	–	–	–	X	–	X	–	X	–	–	–	–	–	X	–	–	–	X	X
Fe oxide (platy)	–	–	–	X	X	–	–	–	–	–	–	–	–	–	X	–	–	–	–	–
Amorphous SiO_2 (leached layers)	–	–	–	–	–	–	–	–	–	–	–	–	–	–	–	–	X	X	–	–
Amorphous SiO_2 (from solution)	X	X	X	X	–	X	X	X	X	–	X	–	–	–	–	X	X	X	X	–

formed in this study is listed in Table 4. For more background on the reactivity of rock-forming minerals as well as glasses, the reader is referred to the following reviews: *Blum and Stillings* [1995], *Brantley and Chen* [1995], *Casey and Bunker* [1990], *Oelkers* [2001], and *White* [1990].

3.2.1. PFR Basalt: Dissolution and Controls on Fluid Chemistry

[32] A strong dependence on pH was observed in the PFR alteration experiments. For example, the Fe-Ti oxides exhibit a particular dependence on initial pH values, where in solutions A and B, the dissolution of the oxides has resulted in large quantities of Fe being released into solution (Figures A1a–A1d). The oxides, while present in the PFR basalt in only about 3.3 wt%, contain nearly 26 wt% of the total Fe budget for the rock system. A strong correlation between Ti and Fe is observed in Figure 1, which shows Ti and Fe in solution with identical slopes close to the bulk Ti/Fe ratio present in the oxides. This suggests that dissolution of the oxides is controlling Fe and Ti release, which indicates that significant ferric and ferrous Fe was released into solution. In solution C, the contribution of Fe to solution from the oxides decreased considerably and was negligible in solutions D and E (confirmed by alteration experiments duplicated on oxide minerals alone), suggesting that the Fe released in the two latter experiments results mainly from pyroxene dissolution (Figures A1e, A1f, and A2a–A2d). Solutions D and E show decreases in Fe concentration by approximately a factor of 10 when compared to experiments C and D, respectively (Figures A1 and A2). This can be attributed to both the decreasing effect of Fe-Ti oxide dissolution and the smaller buffering capacity of these solutions, which are buffered at higher pH values resulting from proton consumption during dissolution, making rapid Fe (II) oxidation more favorable. This is seen in Figure A2e, which plots calculated pH values in solutions A–E. Solution D reaches values between 4 and 6 and Solution E reaches a pH of 8 before the first sampling period. Both of these pH levels favor rapid Fe (II) oxidation [Stumm and Morgan, 1996]. In contrast, the calculated pH values of solutions A, B and C show that the pH has changed minimally as a result of dissolution, indicating that

these solutions can hold substantially more solute before the pH increases to the levels observed in D and E. Speciation calculations from these experiments show that the first solutions in all experiments were undersaturated with respect to any secondary sulfate phases, and therefore precipitation did not occur until the evaporation phases, validating calculated pH values.

[33] An additional control on fluid chemistry in the PFR basalt experiments results from leaching, or ion exchange, of the two silicate minerals, clinopyroxene and plagioclase. Leaching is commonly the first stage of dissolution of pyroxenes and plagioclase, whereby the ionically bonded components of minerals are exchanged for protons at the near surface [Casey et al., 1988; Oelkers, 2001; Schott and Berner, 1983; Stillings and Brantley, 1995]. In solutions A–E, clinopyroxene appears to dissolve in non-stoichiometric proportions. For example, Figure 2 shows

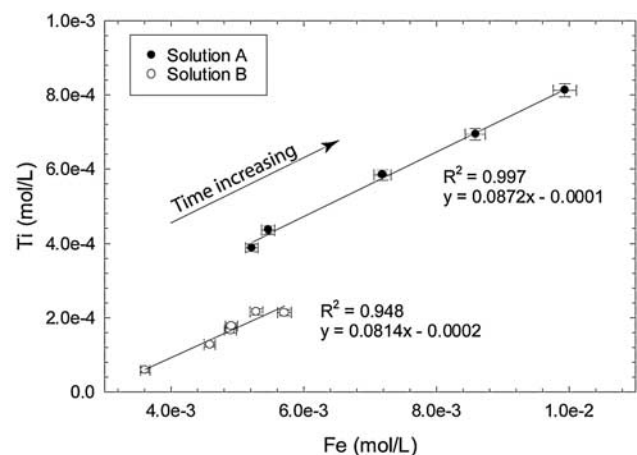


Figure 1. Ti (aq) versus Fe (aq) in PFR basalt solutions A and B. Note the identical slope of the two correlations, indicating that in solutions A and B, Fe-Ti oxide dissolution is controlling Ti and Fe release into solution. The Ti/Fe ratio in the oxides is approximately equal to 0.04.

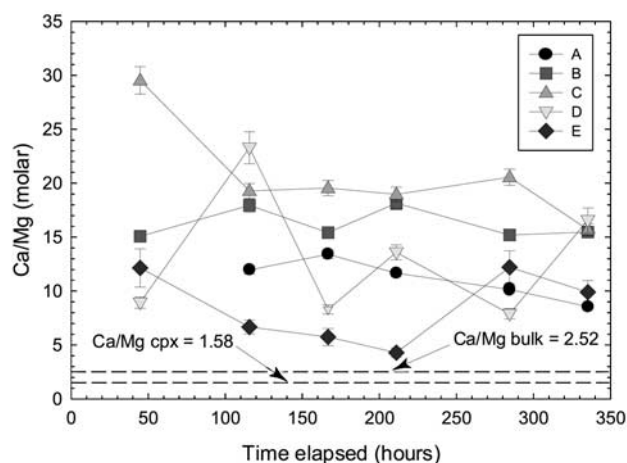


Figure 2. Ca/Mg ratio versus time in PFR basalt solutions A–E. In all experiments, Ca is being released preferentially to Mg. Cpx contains almost all of the Mg of the system, and comparison to the bulk and cpx Ca/Mg values shows that Mg is being retained in the pyroxenes.

that the Ca/Mg ratio in solution is consistently higher than the initial value in the mineral. Plagioclase also contributes Ca to solution, but comparison of the solution Ca/Mg ratios to the ratio present in the bulk basalt shows that Mg is still being retained in the pyroxene (which contains 95% of the bulk Mg) relative to Ca. In addition, the stoichiometry of plagioclase dissolution can be evaluated in Figures A1 and A2, where higher concentrations of Al relative to Na would indicate stoichiometric release because the plagioclase (with a Na/Al ratio of 0.62) effectively contains all of the Na and Al in the basalt (approximately 80% of each). Solution A shows that plagioclase is dissolving close to stoichiometric, where in solutions B–E, Na is consistently higher compared to Al.

3.2.2. PFR Basalt: Secondary Alteration Phases

[34] The experiments discussed above resulted in the precipitation of secondary alteration phases upon evaporation, only one of which could be determined by X-ray diffraction. However, because of the extremely low abundances of some of these phases, only qualitative identification can be determined at present from energy dispersive X-ray analysis. The relative abundances of the secondary phases formed after reaction and evaporation compared to unreacted basalt can be evaluated in Figure 3. Figure 3 clearly shows the relative abundance of secondary sulfates in experiments A, B and C, the lack of abundant sulfates in experiments D and E, and the presence of secondary Fe oxides in experiments D and E.

[35] The PFR basalt experiments resulted in the formation of 3 different Fe bearing sulfate phases. Solution A yielded large amounts (enough to be isolated from the basalt) of what was identified by XRD to be rhomboclase (Figure 4a), a protonated hydrated ferric sulfate ($(\text{H}_5\text{O}_2)^+\text{Fe}^{3+}(\text{SO}_4)_2 \cdot 2(\text{H}_2\text{O})$) found in oxidized sulfide deposits [Jambor *et al.*, 2000]. The presence of this mineral upon evaporation reflects the acidity of the fluid, in that it commonly precipitates in highly acidic fluids by sequestering sulfuric

acid in its structure [Jambor *et al.*, 2000]. As discussed in the previous section, the dissolution of Fe-Ti oxides released a significant amount of Fe, a large proportion of which was likely ferric, which would explain the presence of a ferric Fe-bearing sulfate mineral such as rhomboclase under such acidic conditions.

[36] The second Fe and sulfate-bearing phase of different morphology was identified in both experiments A and B (Figure 3b (inset) and Figure 4a). The phase could not be identified by XRD. However, stoichiometric ratios determined by EDS indicate that the Fe:S ratio is equal to 3:2. There were no other observable elements present in the EDS spectrum other than O, so the Fe:S ratio suggests that if there exists an excess positive charge (caused by ferrous or ferric Fe), provided the S exists as sulfate, then the excess charge is most likely satisfied in the structure by hydroxyl ions.

[37] In solution C, the third Fe and S bearing phase was identified with an elemental Fe:S ratio equal to 1:1. The O to S ratio suggests approximately 11 O per S, which suggests that the phase is $\text{FeSO}_4 \cdot n\text{H}_2\text{O}$, where $n = 6\text{--}7$ (Figure 4b).

[38] The two most concentrated solutions (A and B) also yielded significant amounts of two different Ca-sulfates, gypsum and anhydrite, which were identified on the basis of EDS Ca:S:O ratios (e.g., Figures 3 and 4a). In the less acidic solutions (i.e., C and D), much lesser amounts of only gypsum (Figure 4b) were identified. The presence of these phases results from high levels of Ca present in the fluids prior to evaporation and also because gypsum and anhydrite are among the most insoluble sulfate phases and commonly precipitate first in evaporite sequences [Ptacek and Blowes, 2000].

[39] Amorphous silica was identified by SEM/EDS analysis in significant amounts in experiment A, lesser amounts in experiments B and C, and as small, isolated clusters of cements in experiment D.

[40] In the less acidic conditions used in experiments with PFR basalt (solutions D and E), Fe oxide phases of different morphologies precipitated prior to the evaporation phase of the experiments (Figures 3d, 3e, and 5a). SEM evidence shows secondary Fe oxide phases with both platy and globular morphology. EDS spectra confirm that these phases contain only Fe and O. EDS analyses on the Fe oxide plates yield a Fe:O ratio of 1:2. Therefore it is likely, on the basis of the EDS data as well as morphology, that this phase is goethite ($\alpha\text{-FeOOH}$) (Figure 3d, inset). It is difficult to identify the globular phases on the basis of EDS data alone, because they may be variably hydrated Fe oxide phases, in which case they contain an unknown amount of water.

[41] In addition to the Fe oxide phases mentioned above, a Fe-rich surface layer with “honeycomb” morphology was observed only on the surface of pyroxenes in experiment E. The surface layer is approximately 200–400 nm thick and is most likely composed of poorly crystalline hydrated Fe oxides (Figure 5b). Also, the relationship between the honeycomb structure and other globular Fe oxide phases visible in Figure 5b suggests that the Fe oxide phases were precipitated out of solution after the formation of the layer. Similar ferric oxide surface growths have been reported by several workers investigating pyroxene dissolution under

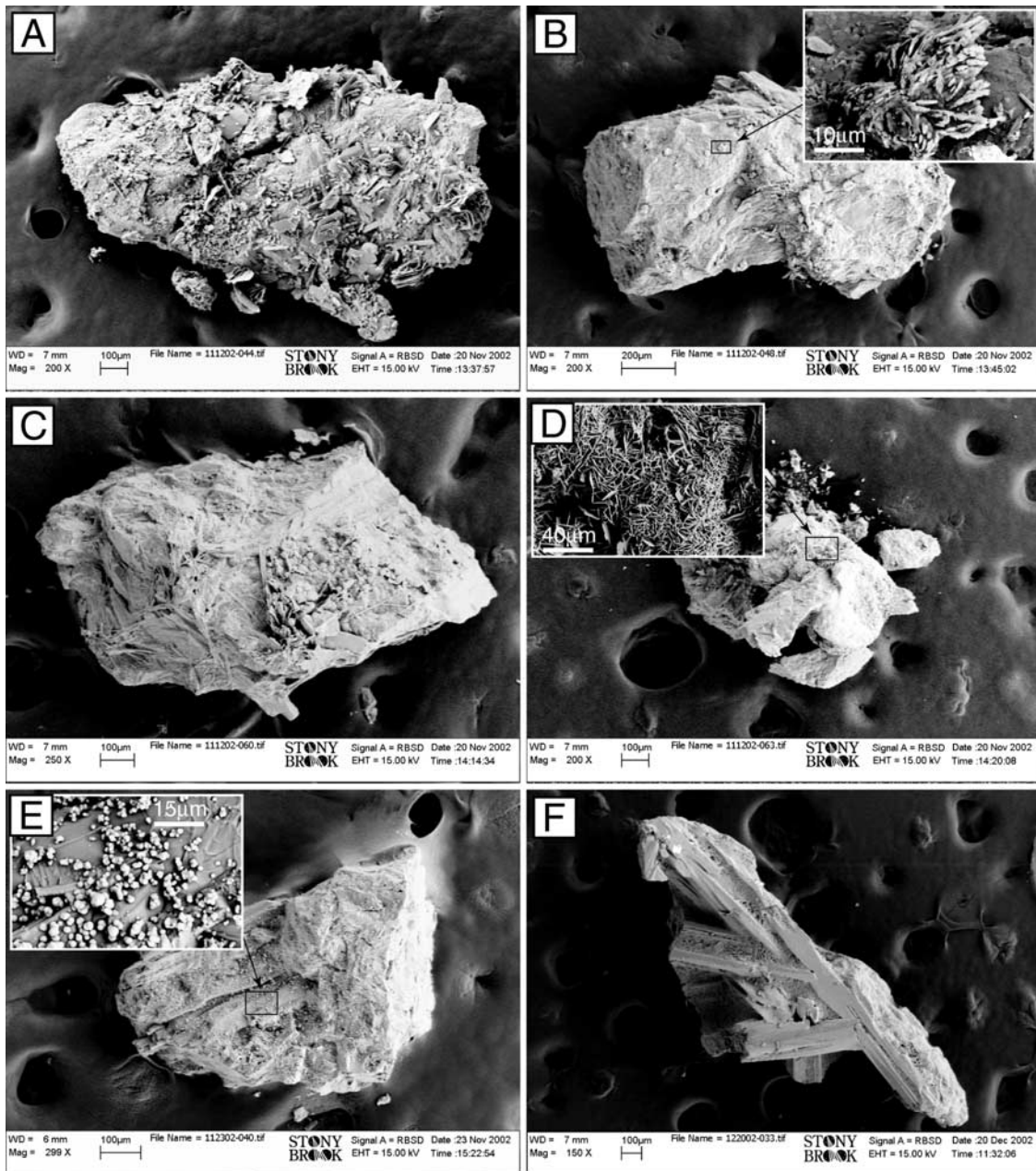


Figure 3. Scanning electron micrographs of PFR basalt: (a) reacted with solution A, (b) reacted with solution B (inset: “hydroxylated” Fe sulfate phase), (c) reacted with solution C, (d) reacted with solution D (inset: goethite), (e) reacted with solution E (inset: hydrated Fe oxides), (f) unreacted.

oxic conditions usually at a pH greater than 4 [e.g., *Schott and Berner*, 1983, 1985].

3.2.3. PFS Basalt: Dissolution and Controls on Fluid Chemistry

[42] One main control on fluid chemistry observed in the PFS basalt experiments results from the presence of olivine in this particular basalt. In solutions A–C, olivine dissolution released large quantities of Fe, Mg and Si (Figure A3). Figure 6 shows that the Mg/Si ratio present in solutions A–D is close to stoichiometric with respect to olivine. Also, the ratios all slowly increase over time and collectively arrive at a value near stoichiometric at the end of the experiments. The Mg/Si ratio in solution E is

significantly lower, which may be controlled by slow oxidation at the surface of olivine, or possibly a result of preferential ion exchange between small amounts of Mg residing in M2 sites of the pyroxenes (requiring 2 protons) as opposed to olivine dissolution (requiring 4 protons). Olivine dissolution is also responsible for increased concentrations of Mn in some solutions, an element present in the olivine at approximately 1 wt%.

[43] In addition to the above controls, the effect of Fe-Ti oxide dissolution can be seen in solution A, where Ti concentration is considerably higher than in solutions B–E, suggesting that Fe is being contributed from oxides in addition to pyroxene and olivine (Figures A3a and A3b).

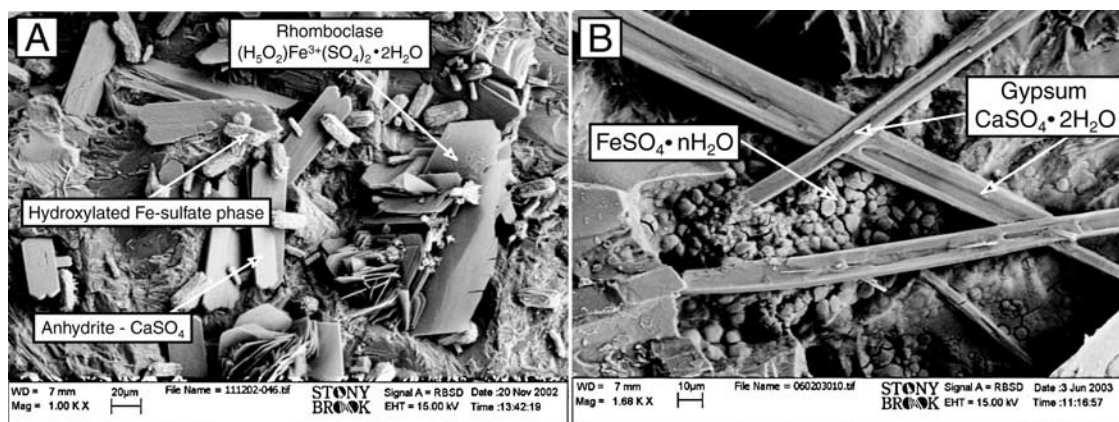


Figure 4. Examples of sulfate alteration phases identified after reaction of PFR basalt with (a) solution A and (b) solution C.

[44] Also, as a result of the relatively high amount of P present in the PFS composition, the olivine and interstitial glass both contained a small amount of P that was released into solution as phosphate, which acidifies the solution. This effect was negligible in all solutions except solutions D and E, which have smaller buffering capacities, causing greater changes in calculated pH.

[45] The plagioclase appears to behave with similar dependence on initial pH to the PFR experiments, dissolving in nonstoichiometric proportions with increasing initial pH values. As evaluated in the PFR experiments, the molar concentrations of Na and Al indicate that plagioclase is dissolving nonstoichiometrically. The Na/Al ratio in plagioclase is 0.4, and because plagioclase contains effectively all of the Na and Al present in the basalt, Na concentrations would be less than half of Al concentrations if stoichiometric dissolution were occurring. It can be verified in Figures A3 and A4 that only in experiment A, where Na and Al concentrations are the same, does plagioclase dissolve the closest to stoichiometric. This indicates that initial ion exchange processes from silicate dissolution (at least with respect to plagioclase) are occurring in these experiments. The stoichiometry of pyroxene dissolution is more difficult to evaluate quantitatively in

the PFS experiments, because Ca is present in significant amounts in both plagioclase and pyroxene, and significant Mg is occupied in the olivine.

3.2.4. PFS Basalt: Secondary Alteration Phases

[46] The relative abundance of alteration phases present upon completion of the PFS basalt experiments is shown in Figure 7. Similar to PFR basalt experiments, solutions A and B have yielded the most alteration phases, where C and D have yielded less and E has yielded the least, producing a correlation with sulfate mineral abundance and initial pH similar to PFR basalt experiments (Figure 3).

[47] The large amounts of Mg released into the fluids resulted in the precipitation of Mg sulfate phases upon evaporation in experiments A and B (e.g., Figure 8). For example, XRD shows the occurrence of hexahydrate ($\text{MgSO}_4 \cdot 6\text{H}_2\text{O}$) in experiments A and B (Figures 9a and 9b). SEM data also show the existence of Mg sulfate phases with variable O contents in these experiments, which may be hexahydrate or possibly an Mg sulfate phase with differing water content.

[48] Fe sulfates were also identified in experiments A and B (e.g., Figure 7a, inset), both with a Fe:S ratio of 1:1 and variable O content, implying variable water content. The average S:O ratio was approximately 10 to 14. The hydra-

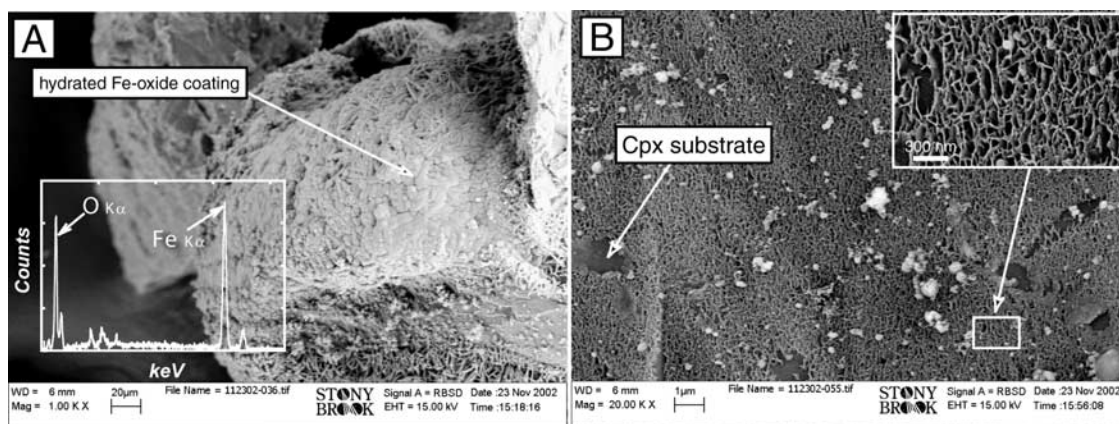


Figure 5. Examples of Fe oxide alteration phases identified after reaction of PFR basalt with (a) solution D (inset: corresponding EDS spectrum) and (b) solution E (inset: high magnification image of surface precipitate).

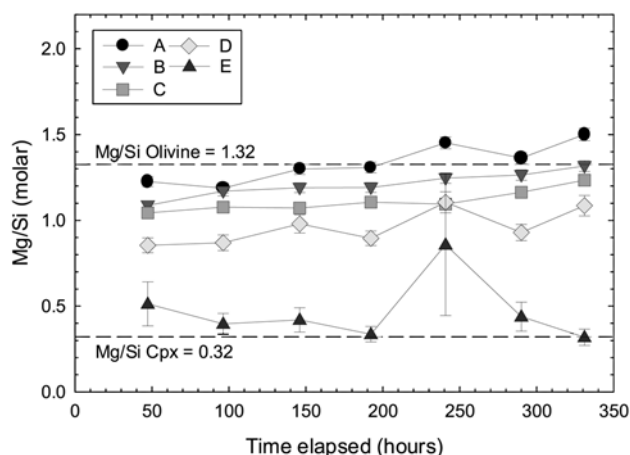


Figure 6. Mg/Si ratio versus time in PFS basalt solutions A–E. Solutions A–D approach close to stoichiometric proportions by approximately 330 hours. Note the lower Mg/Si values present in solution E.

tion state cannot be determined, thus the phase is referred to as $\text{FeSO}_4 \cdot n\text{H}_2\text{O}$.

[49] Gypsum was identified by SEM analysis in experiments A–D on the basis of Ca:S:O ratios. Again, this is consistent with the Ca levels present in solution prior to the evaporation phase, and the relative insolubility of gypsum compared to other sulfates.

[50] In addition, Fe oxide precipitates were identified in experiment B, with the presence of a small P peak in EDS spectra. This suggests that the P may have adsorbed to the surface of these phases after precipitation. This Fe oxide phase is also present in experiment D, but is far less abundant than experiment B. The pH levels again are responsible for rapid Fe oxide formation in this experiment, in that the pH increased from 2 to approximately 8 between 150 and 200 hours of reaction (Figure A4f), which according to speciation calculations was mainly a result of increased solute concentrations in solution. Speciation calculations from these experiments also show that the first solutions in all experiments were undersaturated with respect to any secondary sulfate phases, and therefore their precipitation did not occur until the evaporation phases, validating calculated pH values.

[51] Another Fe bearing phase was identified in experiments B, C and D (Figures 7b, 7c, and 7d, insets). However, instead of S, the phase contained abundant P and O in addition to Fe. The Fe and P in this phase were present in almost equal proportions. It is likely that this phase is a Fe phosphate phase, but could not be identified by XRD. This is consistent with fluid modeling of the solutions in experiment C, for example, where approximately 50% of the P in solution occurs as $\text{FeH}_2\text{PO}_4^+$ prior to evaporation. The precipitation of this phase suggests that the calculated pH values are still somewhat accurate in these solutions, as P was monitored throughout the experiments.

[52] Abundant amorphous silica was observed in experiments A and B, in amounts higher than the PFR basalt experiments. The amorphous silica appears as larger aggregates precipitated on the basalt surface (e.g., Figure 7a). For

comparison, the Si concentrations in PFS basalt solution A were approximately 40 times higher than in that same experiment with PFR basalt. This is a direct result of Si release from olivine dissolution. Small amounts of amorphous silica were also detected in experiments C and D.

3.2.5. PFR Glass: Dissolution and Controls on Fluid Chemistry

[53] Various elemental ratios measured in the fluid suggest that the PFR glass dissolves close to stoichiometric upon interaction with the most concentrated solutions, solution A, B and C (Figures 10a and 10b). Silica dominates this solution, because of the large abundance in the glass itself. Using solutions of weaker acids, the glass dissolves nonstoichiometrically, releasing network-modifier elements preferentially compared to network-forming elements. This is indicated by comparatively low (relative to Ca and Na) Si and Al concentrations in solutions B–E (Figures A5 and A6). The divalent network-modifying elements such as Ca, Fe and Mg behave similarly in all solutions and consequently, their ratios remained constant throughout the 14 day reaction period. For example, Figure 10a shows that Fe and Mg, two divalent network-modifying elements, are being released in close to stoichiometric proportions throughout experiments A–D. The Fe/Mg ratio in experiment E shows that Fe is significantly depleted which is a result of Fe oxidation (see next section), where pH levels reached approximately 8 within the first 50 hours of reaction.

[54] Also, in experiments D and E, the solutions exhibit differences between univalent and divalent network-modifying elements. For example, Figure 10b plots the Na/Mg ratio in solutions A–E. Note in solutions A–C, Na and Mg dissolve close to stoichiometric proportions. In experiments D and E, the Na/Mg ratio increases considerably, suggesting that at weaker acid concentrations, univalent network-modifying elements are preferentially released. This is likely a result of ion exchange processes during the first step of glass dissolution, where exchange of Na requires only one proton as opposed to Ca, Mg and Fe, which require two [Oelkers, 2001; Oelkers and Gislason, 2001], producing preferential release of univalent modifiers. As a result, solutions D and E contain higher proportions of Na and Ca (as well as other network modifiers) in the fluids (Figures A6a and A6c). The actual concentrations of elements (with the exception of Si) in solutions A–E change very little from solution to solution (Figures A5 and A6), suggesting that large variations in initial pH do not control dissolution to the extent observed in crystalline basalt experiments. Comparatively, the reactivity of the PFR glass is less than that of the PFR and PFS basalt, which can be seen from lower solute concentrations as well as minimal changes in the calculated pH of experiments A–D (Figure A6e). The pH values used in these experiments are likely accurate, as all secondary phases were strongly undersaturated throughout the reaction.

3.2.6. PFR Glass: Secondary Alteration Phases

[55] Analysis by XRD failed to detect any secondary alteration phases in any experiments. Analysis by SEM/EDS revealed secondary phases present in very low abundance and in few experiments with PFR glass. This is a result of low amounts of solute dissolved in solution compared to experiments with crystalline basalt. Figure 11

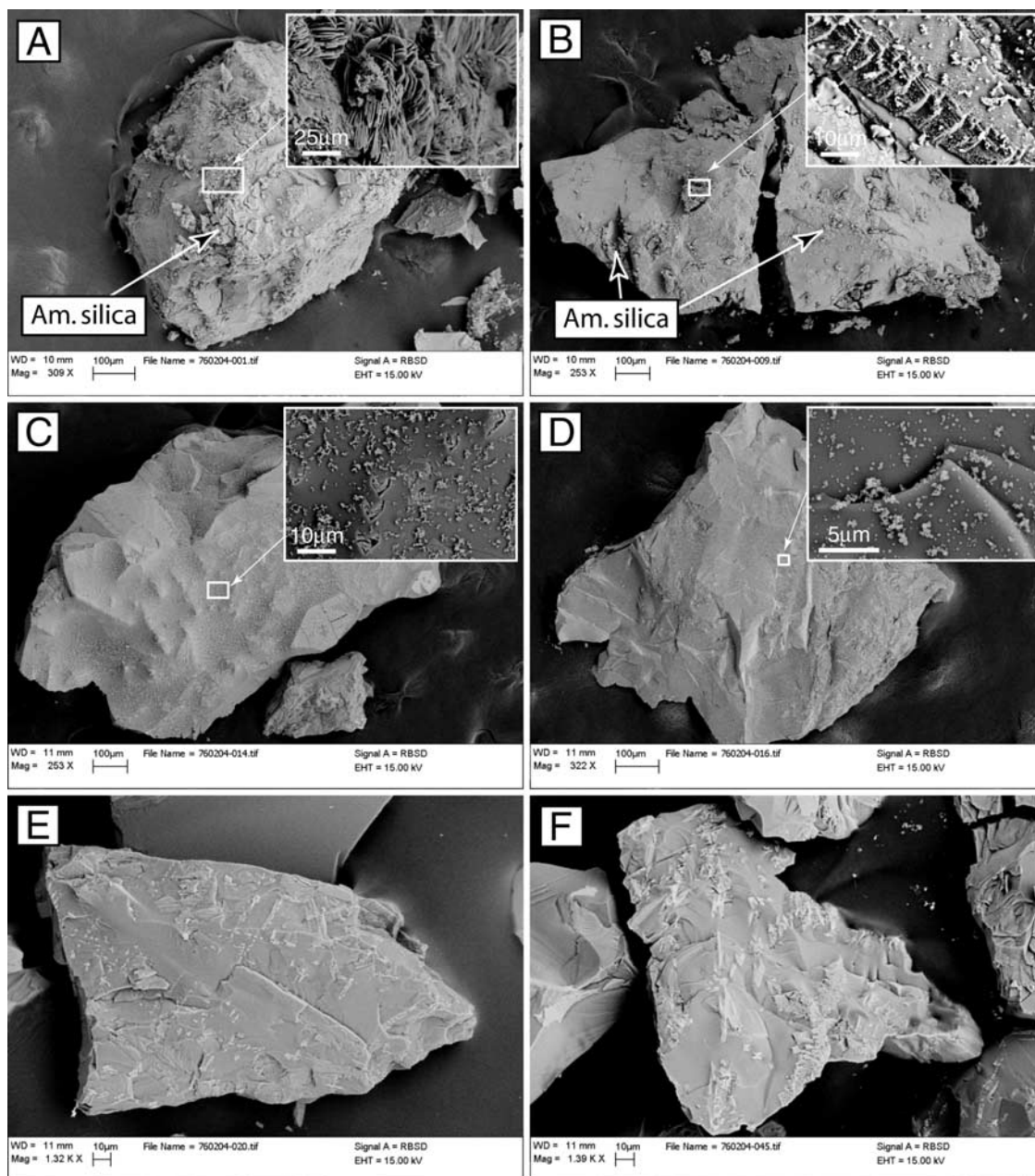


Figure 7. Scanning electron micrographs of PFS basalt: (a) reacted with solution A (inset: $\text{FeSO}_4 \bullet n\text{H}_2\text{O}$), (b) reacted with solution B (inset: Fe oxide (bright) and Fe phosphate (dark) precipitates), (c) reacted with solution C (inset: Fe phosphate precipitates), (d) reacted with solution D (inset: Fe phosphate precipitates), (e) reacted with solution E, and (f) unreacted.

shows the relative abundance of precipitated phases, which (with the exception of experiment E) is difficult to discern because of the small abundance in experiments B and C.

[56] The residual solid from the experiment using solution A was observed under optical microscope to be a white color and of a friable nature (Figure 11a). SEM evidence shows that this material is amorphous silica which cements reacted glass grains together. This is a result of the large amount of Si dissolved in experiment A, which is 2–3 times higher in concentration than experiment B. No other alteration minerals were observed in this particular experiment.

[57] The experiments using solutions A, B and C produced very small amounts of what were identified using SEM as poorly crystalline sulfate cements (Figures 11a–11c) containing Na and Ca, which reflects the fluid chemistry at the beginning of the evaporation process. Small amounts of a fibrous Ca sulfate phase (believed to be gypsum on the basis of SEM constraints) were also observed in experiments using A and B acid concentrations.

[58] SEM analysis indicated what were interpreted to be Fe oxide phases locally precipitated on only a few grains in experiment E (Figure 12). The morphology of these phases is very similar to Fe oxide phases observed from

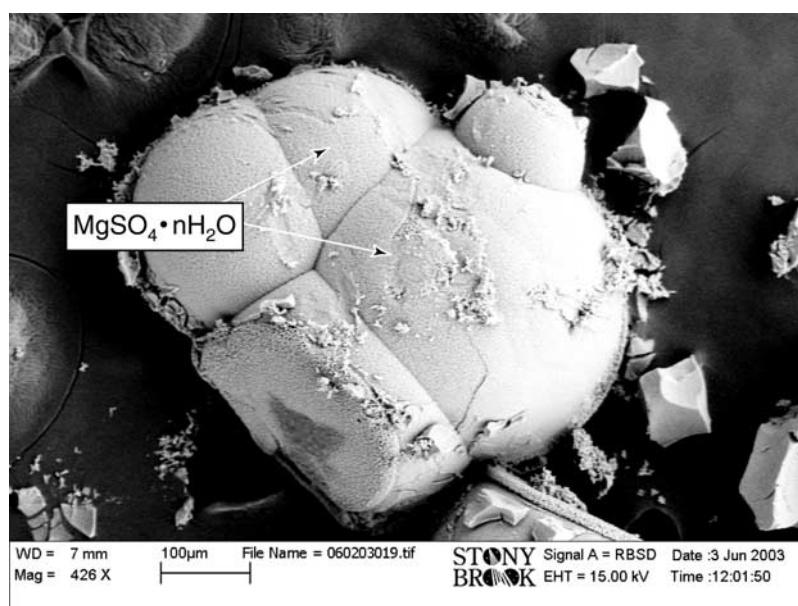


Figure 8. Scanning electron micrograph of PFS basalt showing aggregates of $\text{MgSO}_4 \bullet n\text{H}_2\text{O}$, with a Fe and sulfate bearing coating. The dark area of the particle at the bottom of the image shows where the Fe coating has been removed.

experiments with crystalline basalts (i.e., globular and platy morphology). Also, upon closer inspection of the oxides, the globular phases are composed of aggregates approximately 200 nm in size of even smaller oxide particles (Figure 12, inset).

[59] Halite was also identified having precipitated as 100 nm crystals covering the surface of the glass in experiment E. The occurrence of halite in this experiment is also consistent with the fluid chemistry, where Na was the most abundant solute present in the solution before evaporation.

3.2.7. PFS Glass: Dissolution and Controls on Fluid Chemistry

[60] PFS glass reacted with solution A resulted in almost complete dissolution of the glass in less than 24 hours. When the first fluid sample was taken, the glass appeared as a white gel-like substance of approximately 3 or 4 times the volume the original basaltic glass occupied in the beaker. Consequently, the fluid chemistry of this experiment shows high concentrations of solutes. Figure A7 shows that Fe, Mg, Al and Na, which are all present in concentrations that are at least 4 times higher than the next most abundant element, Si, dominate the fluid in experiment A. It is important to note that the concentrations of Ca and Si in the fluid are comparatively low throughout the duration of the experiment, when compared to experiments B, C and D (Figures A7 and A8). This suggests that either these elements were not leached as extensively as the other elements, or that the saturation states of a silica-bearing phase and a Ca-bearing phase rose rapidly and these phases were precipitated and in equilibrium with the fluid within the first 24 hours before the first fluid sample was taken. The latter seems to be the case as XRD and SEM/EDS of the residual solid suggest (described in the next section).

[61] Figure 13 shows that in experiments A, B and C, the glass is dissolving in stoichiometric proportions with

respect to both univalent and divalent network-modifying elements. In contrast, in experiments D and E, there appears to be preferential release of univalent network-modifying elements as opposed to divalent, consistent with observations in the PFR glass experiments. This is illustrated by the Na/Mg ratio in solution, which increases substantially in experiments D and E (Figure 13). The ratio, however, changes throughout the course of experiment D, most likely a result of precipitation. Nevertheless, these differences in the Na/Mg ratios between experiments are consistent with ion exchange behavior during the initial stage of dissolution with glasses, where the rate of element release is proportional to the element valency [Bouska, 1993; Oelkers and Gislason, 2001].

[62] In experiments D and E, initial increases in solute concentration were followed by sharp drop-offs after 50 hours for experiment D and after 100 hours for experiment E (Figure A8). This is likely a result of precipitation during the reaction phase of the experiment, which, as described in the next section on solid phase analysis, is difficult to resolve due to the nature of the precipitates. However, the solution data show that Al is being released in initially the largest proportion in both experiments D and E (Figure A8). While slightly enriched relative to stoichiometric proportions, Al concentrations are relatively high in experiments D and E, at pH values around 6, which probably initiated precipitation of secondary phases. This would indicate that the calculated pH values for these experiments are possibly not representative, if sulfate or chloride phases have precipitated. In addition, Fe concentrations in these two experiments are comparatively low, suggesting oxidation in solution, which is confirmed by the identification of Fe oxide phases by SEM.

[63] The behavior of the PFS glass relative to the PFR glass in solution indicates that varying bulk composition has a large effect on dissolution and the resulting fluid

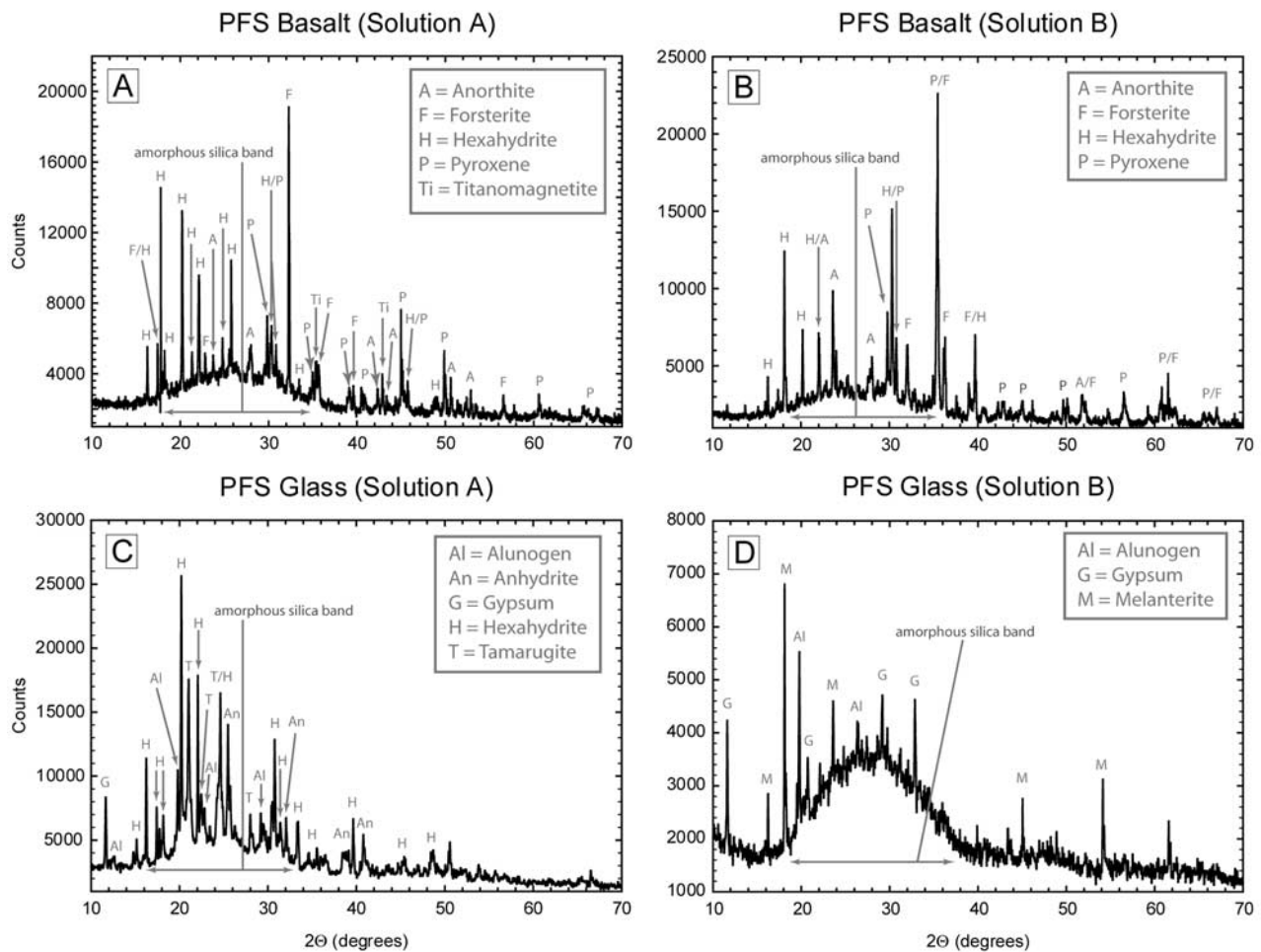


Figure 9. X-ray diffractograms showing the only experiments that yielded identifiable secondary phases (with the exception of PFR basalt, solution A, yielding rhombochase): (a) PFS basalt, solution A, (b) PFS basalt, solution B, (c) PFS glass, solution A, and (d) PFS glass, solution B. Note the larger amorphous silica band present in Figure 9d compared to Figure 9c, indicating the predominance of basaltic glass.

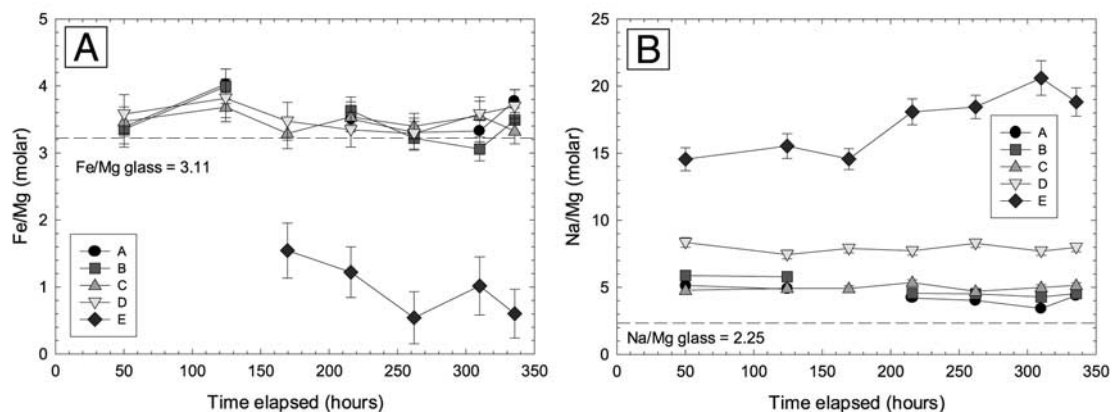


Figure 10. (a) Fe/Mg ratio versus time in PFR glass, solutions A–E. The Fe/Mg ratio is considerably lower in solution E, indicating Fe oxidation. (b) Na/Mg ratio versus time in PFR glass, solutions A–E. The Na/Mg ratio increases in experiments D and E, a result of preferential release of univalent network modifiers.

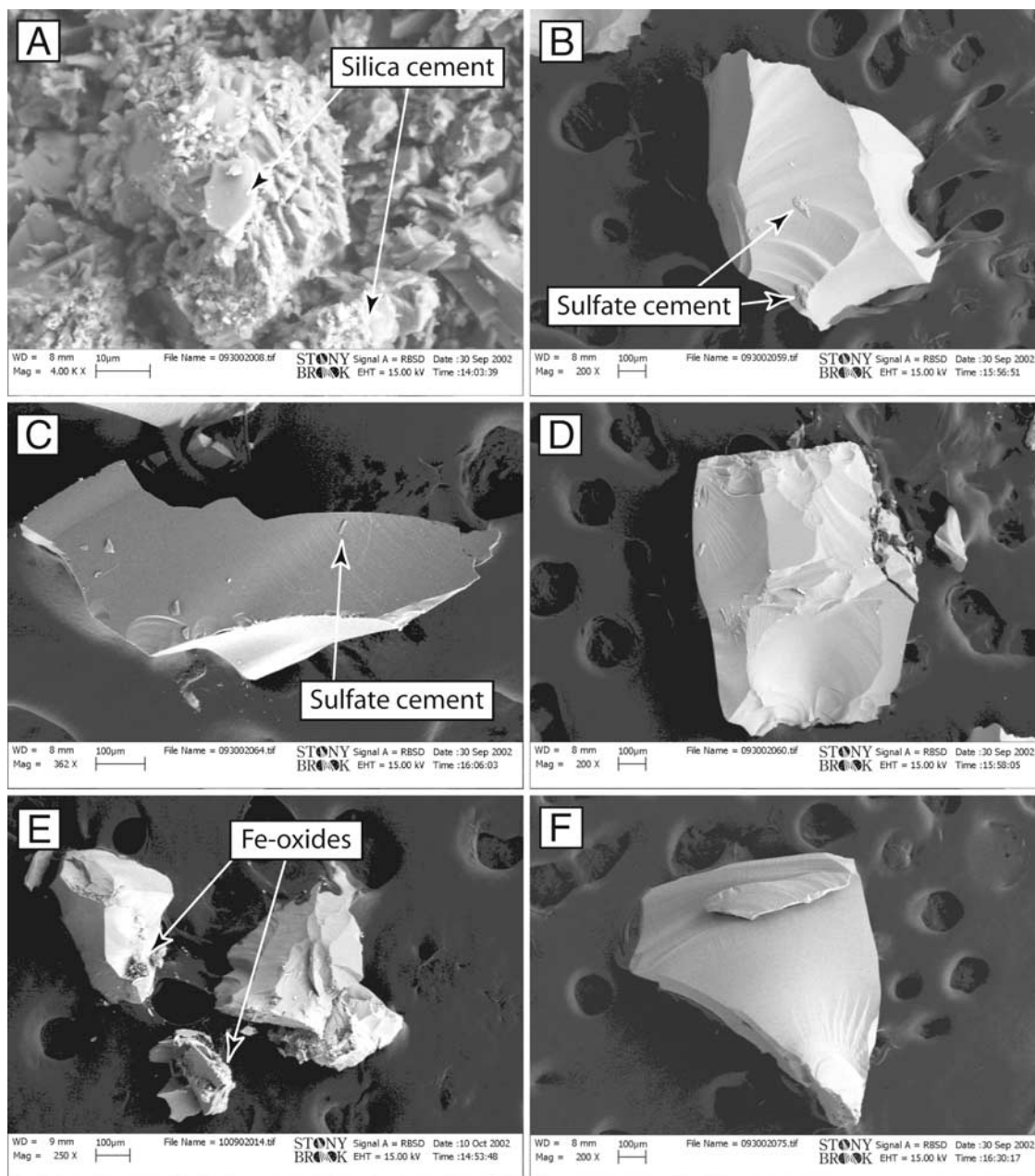


Figure 11. Scanning electron micrographs of PFR glass: (a) reacted with solution A, (b) reacted with solution B, (c) reacted with solution C, (d) reacted with solution D, (e) reacted with solution E, and (f) unreacted.

chemistry of the system. The difference in reactivity of these glasses is a result of the structural characteristics, which are governed by bulk chemical composition. It is important to note that the dissolved silica concentrations in solutions in contact with the PFS glass are in some cases 2 orders of magnitude higher than in the solutions in contact with the PFR glass, while the PFS glass contains less silica in the bulk structure (Figures A5–A8). The implications of these observations to the acid fog model are discussed below.

3.2.8. PFS Glass: Secondary Alteration Phases

[64] Figure 14 shows altered PFS glass grains and the relative abundance and nature of secondary phases formed

during the experiments. The residual solid in experiment A is composed largely amorphous silica, with little primary basaltic glass grains left. The abundance of amorphous silica precipitation decreases from experiments A–E, consistent with solution analyses.

[65] Mg sulfate phases were identified by XRD in experiment A ($\text{MgSO}_4 \bullet 6\text{H}_2\text{O}$, Figure 9) and by SEM/EDS in experiment B ($\text{MgSO}_4 \bullet n\text{H}_2\text{O}$). Experiment B resulted in much less abundant Mg sulfate precipitation, due to approximately an order of magnitude decrease between Mg concentrations in solutions A and B (Figures A7a and A7c). As described above, no Mg sulfate phases were identified in PFR glass experiments, which is due to

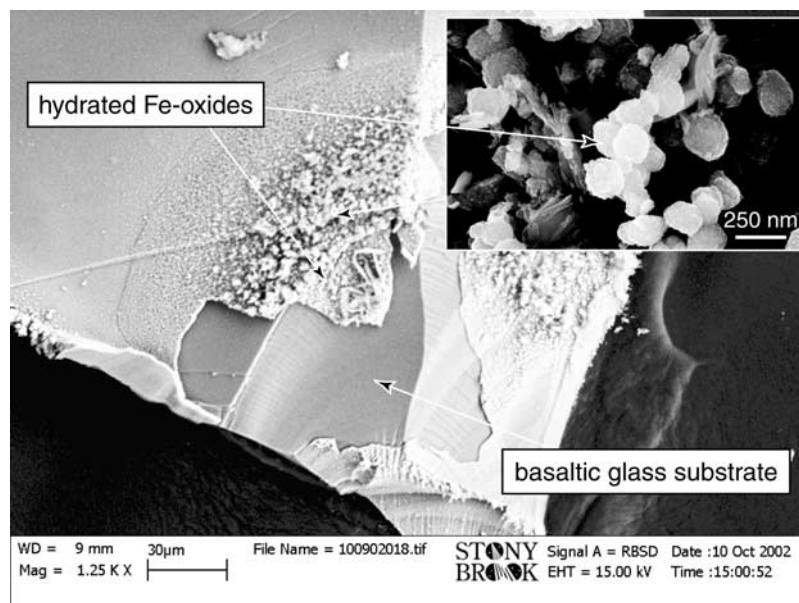


Figure 12. Scanning electron micrograph of Fe oxides formed after PFR glass was reacted with solution E. The inset shows that the oxides are composed of smaller particle aggregates approximately 200 nm in size.

reactivity differences between the glasses as well as differing Mg abundances.

[66] Fe sulfate phases were also identified in experiments A, B and C. Experiment A yielded an Fe sulfate bearing phase not detectable by XRD with a Fe:S ratio of 1:1 and unknown water content. However, XRD analysis of experiment B yielded melanterite ($\text{FeSO}_4 \bullet 7\text{H}_2\text{O}$, Figure 9d). SEM/EDS analysis of Experiment C confirmed a similar phase to that identified in experiment A, but precipitated as smaller grains, approximately 2 μm in size (Figure 14c, inset). No Fe sulfate phases were identified in experiments D and E.

[67] Ca sulfate phases were identified in experiments A–D. XRD analysis identified gypsum and anhydrite in experiment A (Figure 9c). The Ca sulfate phases point to the possibility that precipitation occurred before the drying phase of the experiments, as the fluid data suggest. XRD data also show gypsum precipitation in experiment B (Figure 9d). Also, SEM/EDS analysis identified small amounts of gypsum in experiments C and D (Figure 14d).

[68] One difference with the solid phases formed from reaction with PFS glass is the presence of Al bearing sulfate phases, such as alunogen ($\text{Al}_2(\text{SO}_4)_3 \bullet 17\text{H}_2\text{O}$), identified by XRD in experiments A and B, and tamarugite ($\text{NaAl}(\text{SO}_4)_2 \bullet 6\text{H}_2\text{O}$), identified by XRD in experiment A (Figures 9c and 15). The presence of Al-bearing sulfate phases is a result of larger concentrations of Al released from the glass during dissolution as opposed to crystalline basalt, where a significant fraction of Al is bound in less rapidly dissolving phases (i.e., plagioclase) [Oelkers, 2001; Oelkers and Gislason, 2001].

[69] Fe oxide phases were identified by SEM/EDS in experiments D and E only. The oxides precipitated in experiment D as small globules approximately 200–300 nm in size (Figure 16a). The Fe oxide phases that precipitated in experiment E appeared as smaller aggregates

composed of plates 100–200 nm in size. The Fe oxide phases present in experiment E were also precipitated inside what appears to be a porous surface layer of glass that has a bulk composition similar to the basaltic glass substrate (Figure 16b). This unidentified phase, or any combination of phases identified in experiment E may have been the precipitate suggested to form in this experiment from the solution data. In addition, experiment E resulted in the formation of a Na bearing sulfate phase, too small to be identified with reliable EDS analyses (Figure 16a).

[70] SEM data also show the presence of a layer covering the entire surface of glasses in experiments using B and C

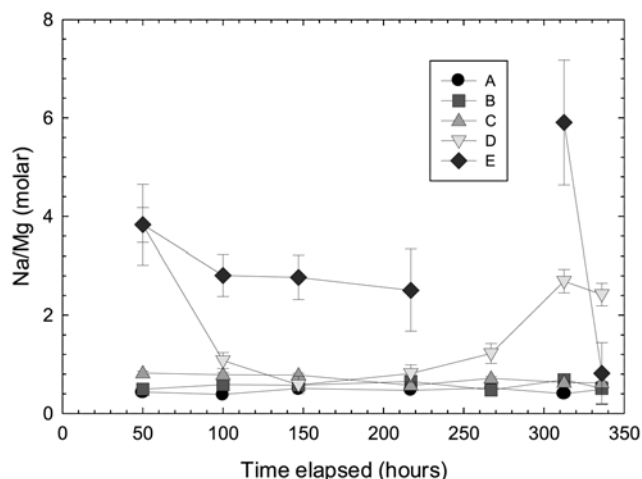


Figure 13. Na/Mg ratio versus time in PFS glass, solutions A–E. Solutions D and E show higher Na/Mg ratios in solution, indicating preferential univalent network modifier release.

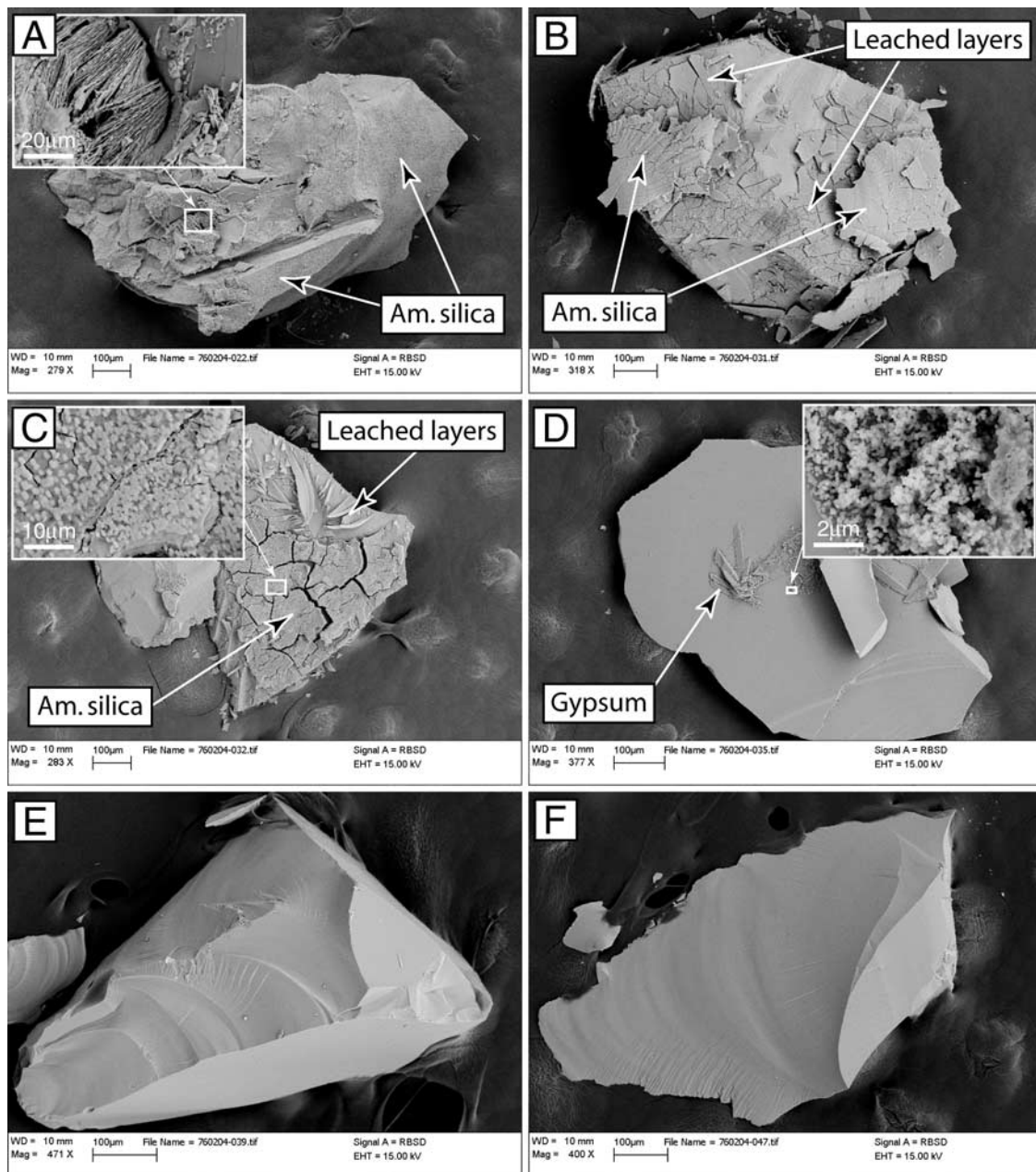


Figure 14. Scanning electron micrographs of PFS glass: (a) reacted with solution A (inset: tamarugite), (b) reacted with solution B, (c) reacted with solution C (inset: Fe sulfate precipitate on amorphous silica), (d) reacted with solution D (inset: hydrated Fe oxides), (e) reacted with solution E, and (f) unreacted.

solutions. This layer at its thickest is approximately 10 μm , by SEM analysis. The thickness of these layers likely represents the extent of leaching of the glass surface during the course of the experiments. The layers are rich in Si and O and contain minor amounts of Al and Ti. These layers are also fragile and flake off the glass surface under gentle contact with tweezers during the specimen mounting process. When the layers flake off, they expose fresh basaltic glass (determined by EDS) underneath. It is important to distinguish between leached layer formation and amorphous silica precipitation from solution, which was identified in abundance in experiments A, B and C (Figures 14a–14c). This particular precipitate appears much thicker than leached layers and only covers specific areas of

glass grains. In some cases, silica precipitated from solution covers areas of leached layers. The differences in these two silica phases can be observed in Figures 14b and 14c.

4. Discussion and Conclusions

4.1. Primary Mineralogy and Reactivity

[71] The results and observations discussed in this study show that the bulk chemical composition and the primary mineralogy are key factors in the evolution of fluids in contact with Martian basalt and basaltic glass. However, several factors control the reactivity of primary basalt and glass and have the potential to be important to the acid fog model.

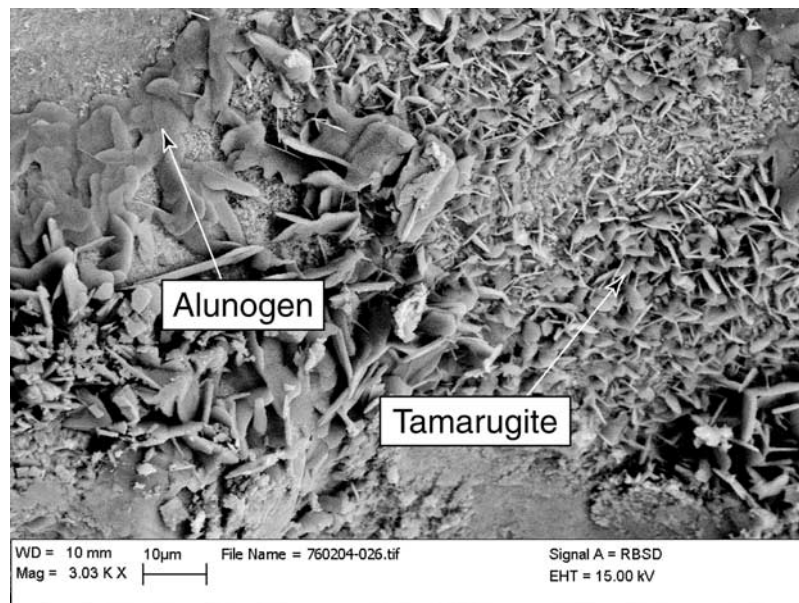


Figure 15. Scanning electron micrograph of PFS glass after reaction with solution A.

[72] Most notably, aside from controlling the resulting modal mineralogy in crystalline basalts, bulk composition has shown to be critical in the reactivity of basaltic glasses in this study. Comparison of the reactivity of PFR and PFS glasses shows that the PFS glass, with approximately 9 wt% less SiO_2 has released significantly more solute than experiments with PFR glass (Figures A5–A8). Also, the extent of reaction can be seen with the formation of leached layers on the surface of the PFS glass (Figure 14) and the resulting assemblages of secondary phases, which are significantly more abundant opposed to the PFR glass (Figures 9c, 9d, and 14–16). These differences in reactivity can be attributed to the glass structure, which is controlled by composition.

[73] There is substantial evidence for the compositional control on natural glass reactivity, both in natural and experimental settings [Bouska, 1993; Glass, 1984; Jantzen and Plodinec, 1984; Oelkers, 2001; Oelkers and Gislason, 2001]. For example, Jantzen and Plodinec [1984] intro-

duced a thermodynamic model of glass dissolution based on the number of nonbridging oxygens present in glass, which correlates inversely with the amount of SiO_2 present. After analyzing a range of natural and synthetic glasses, they found a direct correlation with increased mass loss (spanning several orders of magnitude) resulting from dissolution and the increasing percentage of nonbridging oxygens present in the glass. In addition, Glass [1984] provided natural evidence for this trend by analyzing a large number of microtektite glasses from both deep sea and continental environments in order to determine the amount of dissolution each glass had experienced. The SiO_2 content of the glasses sampled ranged from 45 to 82 wt%. Glass [1984] found that the intensity of dissolution increased systematically with decreasing silica content. This trend in glass reactivity is important to the acid fog model, as it controls the solution composition, alteration phase precipitation and leached layer formation of basaltic glass.

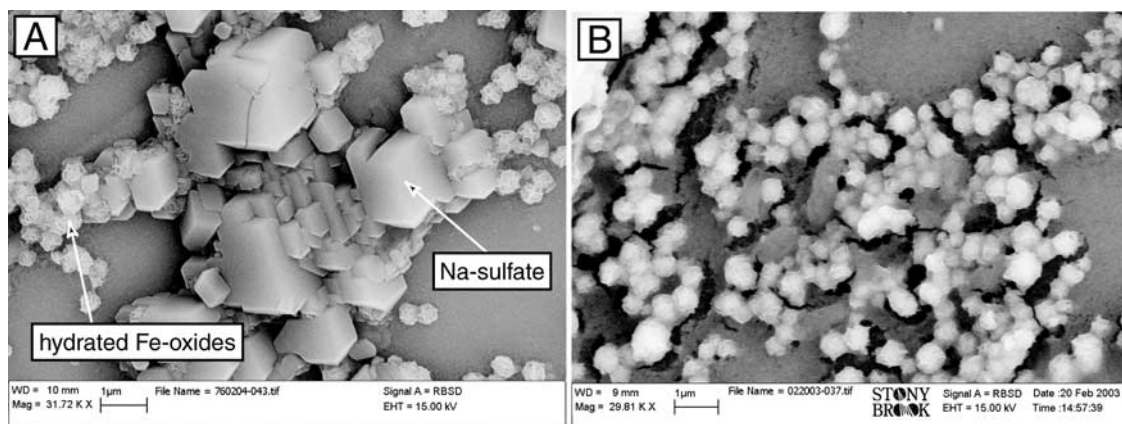


Figure 16. Scanning electron micrographs of PFS glass after reaction with solution E. (a) Na and sulfate bearing phase and submicron sized Fe oxide phases. (b) Fe oxide phases precipitated in unidentified, porous matrix material resembling glass surface.

In addition, differences of this magnitude in the dissolution rate require that the residence time of lower silica glasses (similar to the PFS composition) be significantly less than those containing higher amounts of silica.

[74] Results from this study indicate that physical weathering on Mars, an important component of the surface oriented acid fog model, may also control the reactivity of primary basalt and glass. Solution data from this study indicate that within the first 50 hours of interaction, high element concentrations in solution are reached (Figures A1–A8), despite efforts to remove reactive ultra-fine particles. This is likely the result of the initial high reactivity of primary silicate minerals after grinding. This effect has been observed by several researchers and has been attributed by many to be the result of the formation of disrupted mineral surfaces with an increased number of defects induced by mechanical grinding [Eggleson *et al.*, 1989; Holdren and Berner, 1979; Knauss *et al.*, 1993; Petrovich, 1981]. Also, there is substantial theoretical and observational evidence that dissolution occurs preferentially at such defects produced at mineral faces [see Lasaga, 1998, and references therein]. It is for this reason that several workers etch mineral samples in acid after grinding before performing quantitative dissolution studies [see Eggleson *et al.*, 1989]. In light of this evidence, in the context of the acid fog model, it is likely that intense physical weathering of the surface material on Mars may have enhanced the reactivity of the basalt with respect to short-term dissolution. This ongoing process would have enabled short, intermittent reaction of the basalt with fluids to be more effective, releasing short bursts of solute into solution before evaporation.

[75] It is evident when comparing solution data with solid analyses performed in this study that the stoichiometry of dissolution dictates which secondary phases are formed upon evaporation. The solution data indicate that the primary silicate minerals and glasses dissolve close to stoichiometric when in contact with very acidic solutions (i.e., solutions A and B) and nonstoichiometric when in contact with less acidic solutions (i.e., C–E). In stagnant fluid systems, which are the most relevant to the acid fog model, the pH will largely determine the stoichiometry of solution, where elemental ratios will be “set” by the initial reactivity, changing little until evaporation takes place. For stagnant systems with low buffering capacities (i.e., solutions D and E), initial ion exchange occurs which consumes protons, buffers the solution at higher pH (approximately 6 to 8, as observed in this study), and slows dissolution until evaporation.

[76] An additional factor shown here to be important to the acid fog model is pH, because it controls dissolution rate, Fe (II) oxidation rate (when molecular O₂ is the oxidant), it indirectly effects the stoichiometry of the solution through buffering capacity and controls the precipitation of alteration phases before and during evaporation. Low pH values can create an environment where several unusual sulfate minerals are precipitated in abundance. For example, under conditions similar to the fluid conditions of acid mine drainage from sulfide oxidation (i.e., the resulting fluids in experiments A and B for the two basalt systems and the PFS glass), significant quantities of sulfate and metals such as Fe, Mg and Al are produced [Bigham and

Nordstrom, 2000; Jambor *et al.*, 2000]. The fluids in these systems have a high buffering capacity and effectively retain the same pH. This leads to the precipitation of sulfate minerals such as rhomboclase and melanterite, which either precipitate directly from acidic pH fluids, or require that significant leaching of metals occur to precipitate. Conversely, weak acids are buffered at high pH values by basalt dissolution, which increase aqueous silica solubility as well as the saturation state with respect to several alteration minerals. While pH conditions of past environments on Mars are currently unconstrained, the identification of specific sulfate minerals or clays on the surface may serve as markers for pH conditions upon precipitation.

[77] Lastly, an important caveat to the acid fog model is fluid-to-rock ratio. The experimental results described above are limited to fluid-to-rock ratio of 10 in order to characterize the important chemical reactions and products experimentally. However, with lower fluid-to-rock ratios (significantly less than 1), such as those encountered with aerosol-basalt interaction, the mechanisms of mineral and glass dissolution are not anticipated to change. Such fluid-to-rock ratios will largely control secondary mineral abundance, with smaller amounts of fluid and less alteration product formed per reaction step along with the formation of phases with poor crystallinity. More work is needed to characterize aerosol-basalt weathering, but the current study provides a framework for which these reactions may be better understood.

4.2. Secondary Mineralogy: Implications for the Martian Surface

[78] An evaluation of the variety of putative secondary alteration phases produced during these experiments (Table 4) indicates that relevant composition and mineralogy are critical in the investigation of the weathering of Martian analog basalt. The resulting sulfate, Fe oxide and silica phases are each important to the secondary mineralogy proposed by the acid fog model and are discussed in greater detail in this section.

4.2.1. Sulfate Mineralogy

[79] The experiments performed in this study have resulted in a complex assemblage of secondary minerals. In particular, the sulfate phases produced in these experiments have important implications for the secondary mineralogy of the Martian surface if a process similar to the acid fog model was operating in the past. However, questions still remain as to the fate of Ca during acid fog processes in light of evidence presented here, showing that gypsum and anhydrite precipitate in several instances [Banin *et al.*, 1997; this study]. There is conflicting evidence between chemical analyses of the Martian surface (from Pathfinder data and remote sensing data) and studies that report Ca sulfate formation resulting from aqueous alteration of Martian meteorites [e.g., Bridges *et al.*, 2001]. Clinopyroxene and plagioclase are important components of the primary mineralogy of Mars, both of which may contribute calcium to fluid systems resulting from initial ion exchange. Whether a different sink on the Martian surface for Ca other than gypsum remains undiscovered or whether gypsum (or other Ca phases) may be present but not detected leaves this question open to interpretation and more investigations are certainly necessary.

[80] Several workers suggest that Mg sulfates may explain the correlation between Mg and S in the Pathfinder soils [e.g., *Bell*, 1996; *Clark*, 1993; *Rieder et al.*, 1997]. Hexahydrite was detected in these experiments (Figure 9) and appears to be formed by olivine dissolution releasing substantial quantities of Mg into solution (Figures A3 and A4). Of the synthetic pyroxene compositions in these experiments, none appear to release enough Mg during the short timescales used to produce any appreciable amounts of Mg sulfate phases upon evaporation. If Mg sulfates are an important secondary component, as the geochemical signature in the Martian soil suggests, then olivine is almost certainly required for their formation by acid fog processes, at least during short reaction timescales.

[81] Several Fe sulfate phases are also viewed as potential components of the secondary mineralogy of Mars [e.g., *Bell*, 1996; *Bishop and Murad*, 1996]. The rapid release of ferrous iron into solution from Martian basalt and the transient nature of aqueous sulfate fluids during acid fog processes may create an ideal environment for the precipitation of Fe sulfate phases. The nature of the Fe sulfate phases depends on the redox state of the system, potentially creating trivalent Fe sulfate salts either by oxidation or, in highly acidic fluids where Fe oxidation is suppressed, dissolution of ferric Fe bearing mineral phases (i.e., solutions A and B reacted with PFR basalt). The Fe sulfates that have formed in these experiments include rhomboclase, melanterite and a hydroxylated Fe sulfate phase, which is undetectable by XRD (Figures 3, 4, and 9). Fe sulfates are a common secondary component of these experiments with high-Fe basaltic compositions, and therefore it is likely that they would exist on the surface of Mars if the acid fog model were important in the past.

[82] Aluminum sulfate minerals were only identified in experiments involving the weathering of basaltic glass (Figures 9, 14, and 15). The weathering of the PFS glass releases Al in much greater proportions as opposed to crystalline basalt where Al is bound in plagioclase, which dissolves at a much slower rate. As discussed above, the silica content of glass controls reactivity, and consequently Al release to solution. In light of evidence from this study, the precipitation of Al sulfate minerals resulting from acid fog processes on Mars may be the most dependent on the proportion of basaltic glass available to weather extensively.

4.2.2. Iron Mineralogy

[83] As discussed above, secondary Fe oxide phases have been identified in some of the experiments conducted in this study. These particular experiments were duplicated with solutions spiked with 10 ppm HgCl_2 to sterilize the system and ensure that the precipitation of Fe oxides was not microbially mediated. All duplicated experiments yielded secondary Fe oxide phases. As discussed above, Fe oxidation is the most dependent on the pH of the system. The experiments yielding Fe oxides have all reached calculated pH values of greater than 4, a process that obeys a rate law of Fe (II) oxidation that is second order dependent on pH and first order dependent on O_2 fugacity [*Stumm and Morgan*, 1996]. Also, the nature of the Fe precipitates agrees well with proposed products of the acid fog model [*Banin*, 1996; *Banin et al.*, 1997] in that they are poorly crystalline, having precipitated both as small clusters only several hundred nanometers in size (Figures 5 and 16), and as

layers 200 nanometers thick observed on pyroxene surfaces (Figure 12b). These poorly crystalline Fe oxide phases could be easily stripped off mineral surfaces and distributed into the Martian sediment. This stresses the importance of the presence and relative proportions of ferromagnesian silicate minerals when testing models of Martian soil formation.

4.2.3. Silicate Mineralogy

[84] Amorphous silica was observed in several forms during the course of these experiments, including cements, discrete grains and as residual leached layers. Precipitation of amorphous silica as cements and grains has resulted from high concentrations of silica released in the fluids. Experiments using low pH solutions release substantial quantities of aqueous silica, which quickly reach saturation with respect to amorphous silica. The experiments with PFS basalt have resulted in significant silica release to solution, mainly due to olivine dissolution.

[85] Another important observation in several of the experiments described above is the formation of residual silica-rich coatings resulting from basaltic glass dissolution. The coatings formed from the basaltic glass experiments cover the entire surface of the glass in most instances. During the nonstoichiometric dissolution of the glass, the silicate structure or network is left behind while other constituents are preferentially released to solution. This forms a silica rich layer on the surface of the material, which can approach several microns thick. The thickness of these layers is proportional to the extent of dissolution, and hence pH of the solutions used in the experiments. In particular, the PFS basaltic glass used in the experiments described above results in a substantial production of these layers upon reaction with various acidic fluids (Figure 14). These results are consistent with the suggestion that high silica features, observed spectroscopically on the surface of Mars, may be a result of amorphous silica liberated from basalt alteration [*McLennan*, 2003].

[86] A variety of clay minerals have been proposed to be of importance on the surface of Mars (see *Banin et al.* [1992] for review), and recently, *Wyatt and McSween* [2002] have modeled surface Type 2 regions of Mars as containing up to approximately 30% clay minerals. No clay minerals were detected in the experiments performed in this study using the analytical methods outlined above. The lack of clay mineral formation is most likely a consequence of the short reaction times used in these experiments. Even though clay minerals are common in aqueous systems (sometimes resulting from small degrees of basalt alteration [e.g., *Casey et al.*, 1993]), the lack of clay minerals in these experiments remains consistent with the acid fog model invoking basalt weathering that does not lead to the formation of well crystalline clay minerals [*Banin*, 1996; *Banin et al.*, 1997]. As a result of this mechanism, the silica released from basalt weathering remains in an amorphous (or perhaps short-range ordered) form, as indicated by the ubiquitous formation of amorphous silica products in the experiments discussed above.

4.3. Conclusions

[87] In summary, the results described in this study have several important implications for the acid fog model as well as other models involving alteration of Martian basalt and glass by acidic fluids. This study has demonstrated the critical importance of primary bulk composition and min-

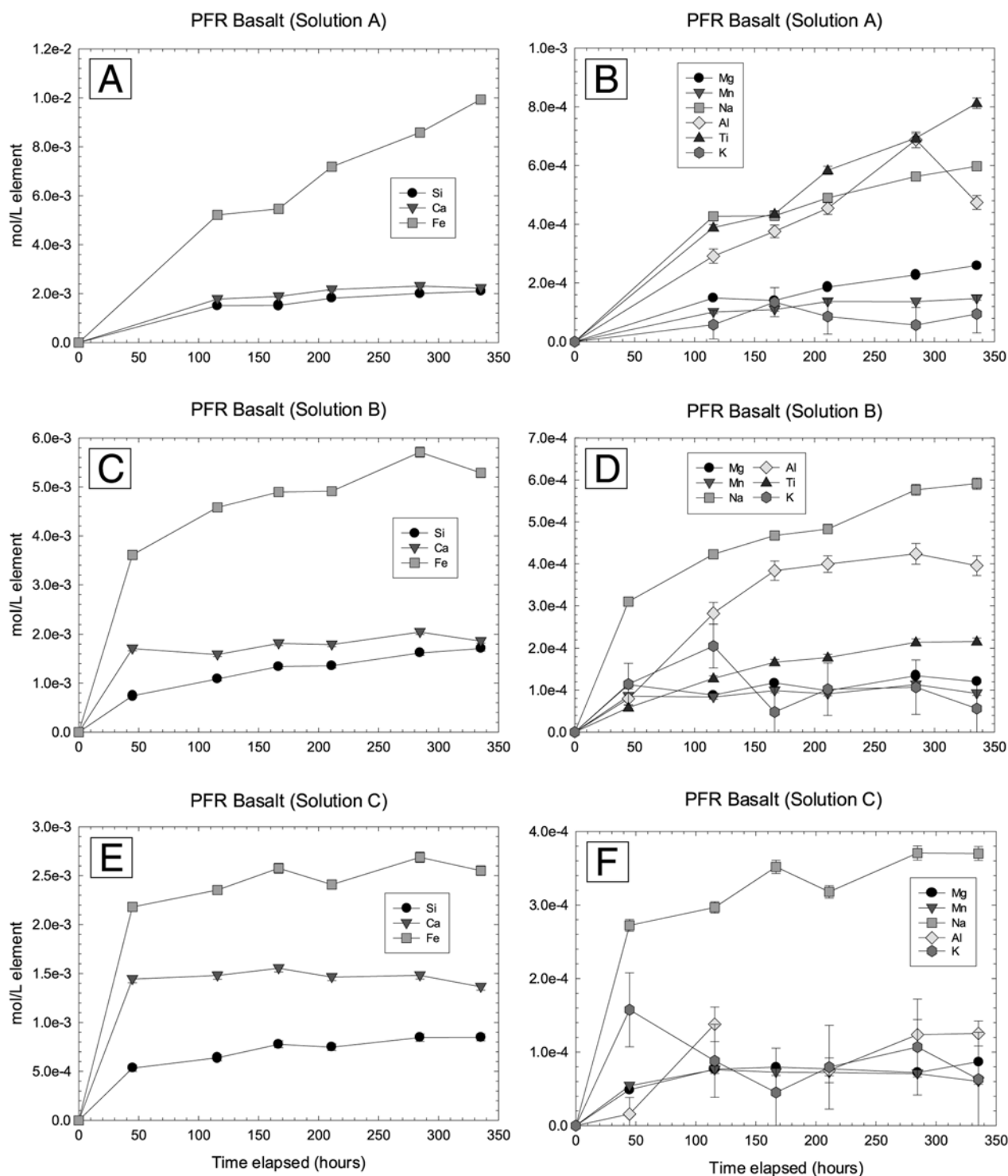


Figure A1. Major element solution concentrations during reaction with PFR basalt and (a and b) solution A, (c and d) solution B, and (e and f) solution C.

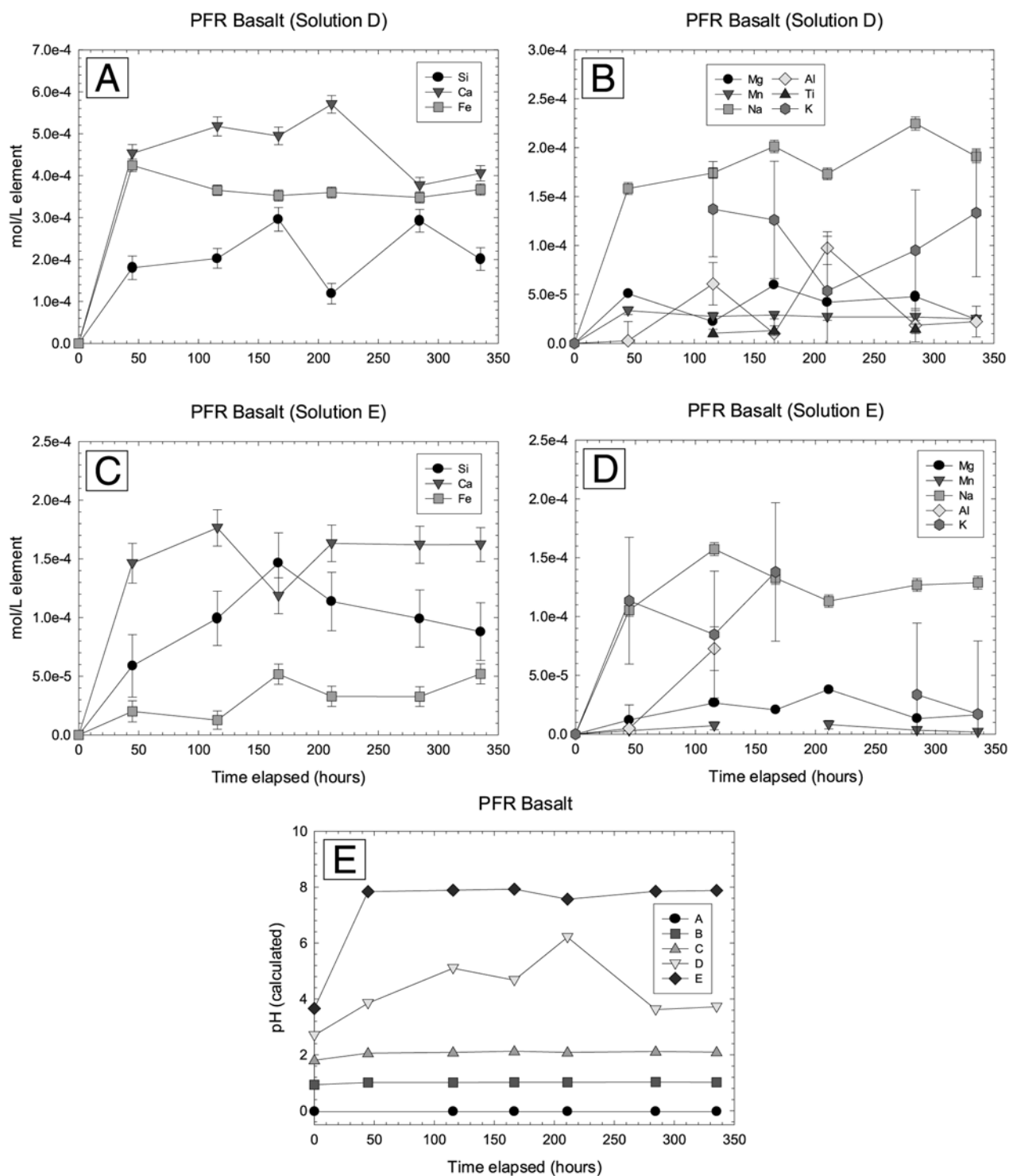


Figure A2. Major element solution concentrations during reaction with PFR basalt and (a and b) solution D and (c and d) solution E. (e) Calculated pH values during reaction.

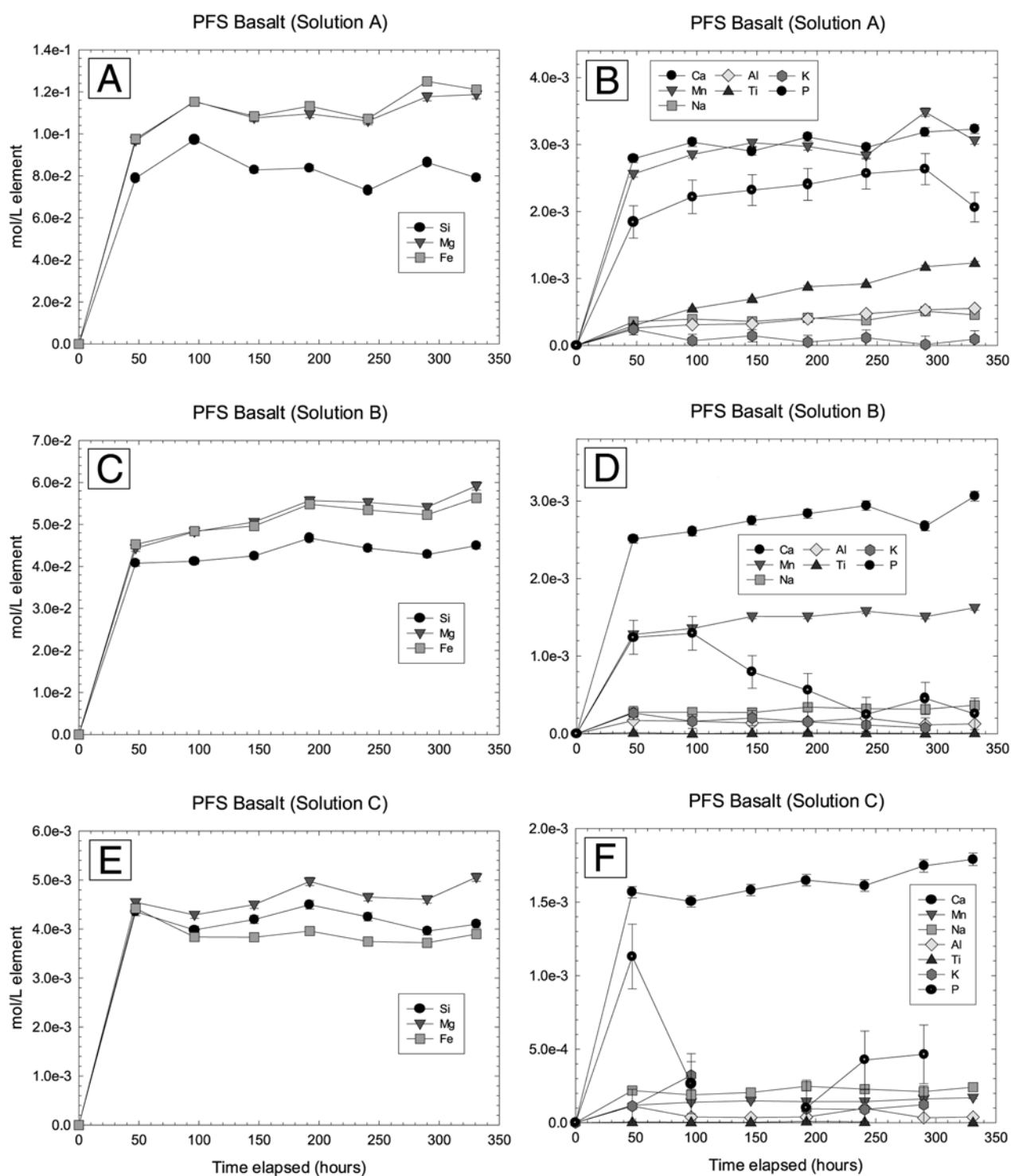


Figure A3. Major element solution concentrations during reaction with PFS basalt and (a and b) solution A, (c and d) solution B, and (e and f) solution C.

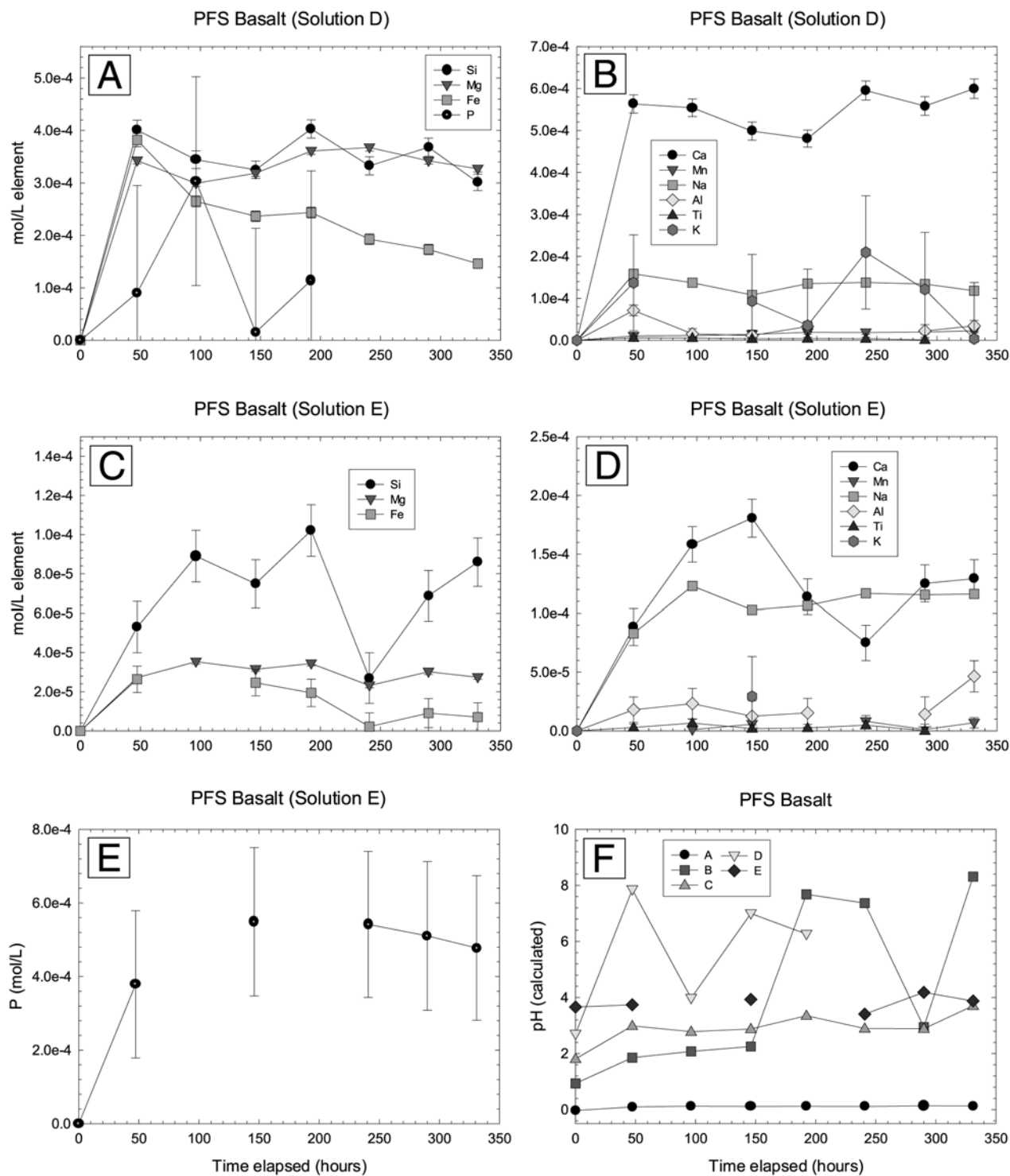


Figure A4. Major element solution concentrations during reaction with PFS basalt and (a and b) solution D, and (c and d) solution E. (e) Phosphorus concentration versus time. (f) Calculated pH values during reaction.

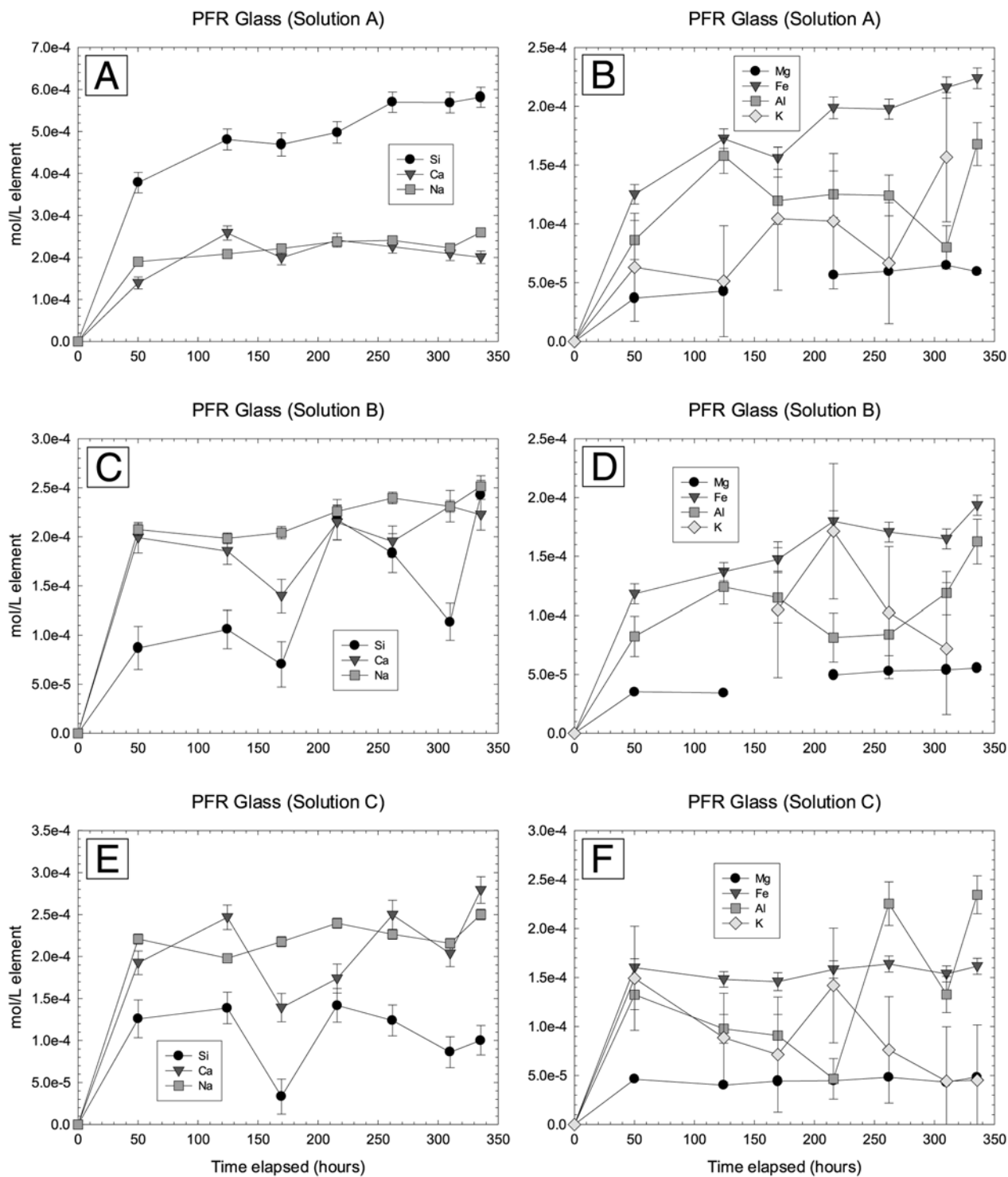


Figure A5. Major element solution concentrations during reaction with PFR glass and (a and b) solution A, (c and d) solution B, and (e and f) solution C.

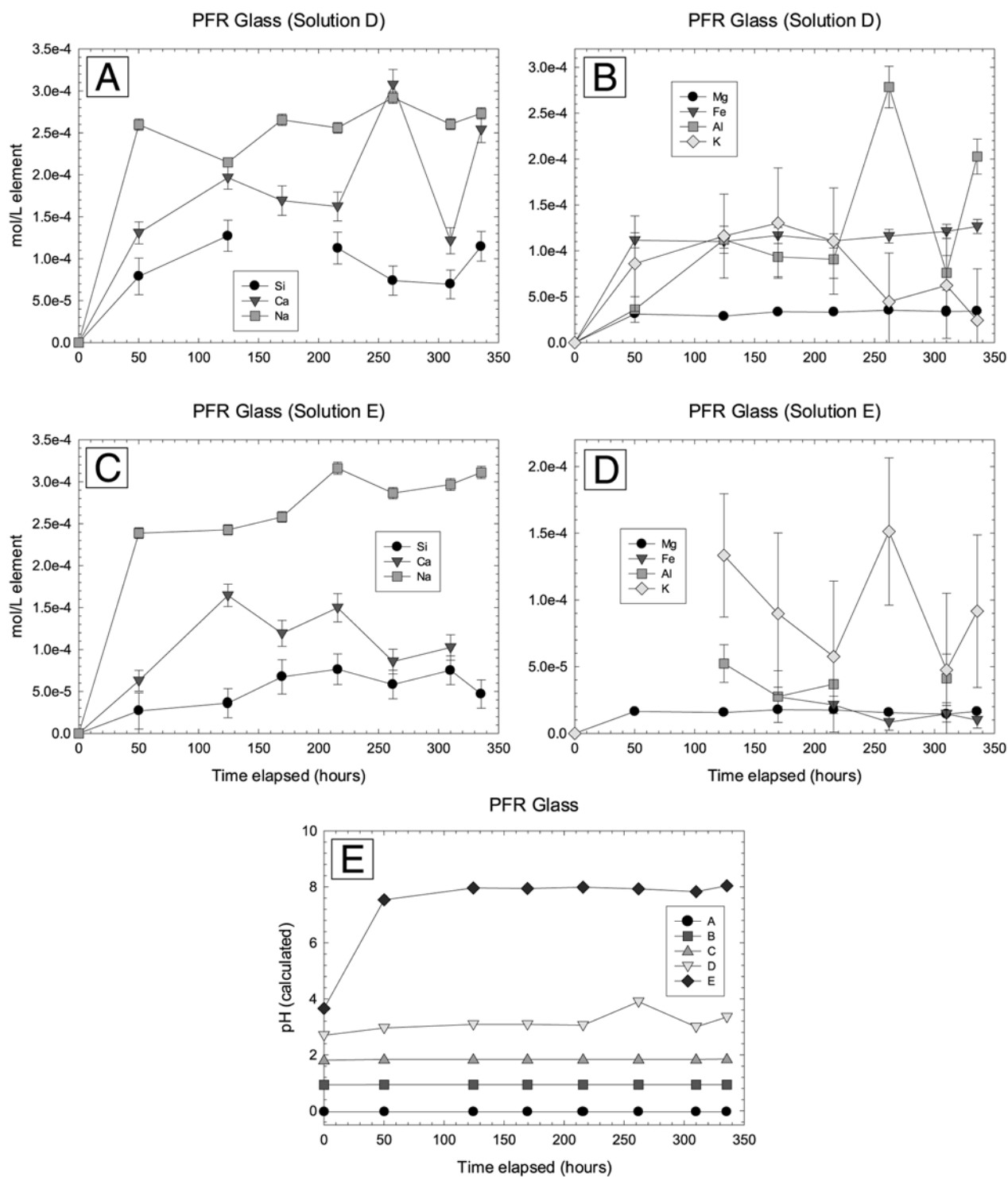


Figure A6. Major element solution concentrations during reaction with PFR glass and (a and b) solution D and (c and d) solution E. (e) Calculated pH values during reaction.

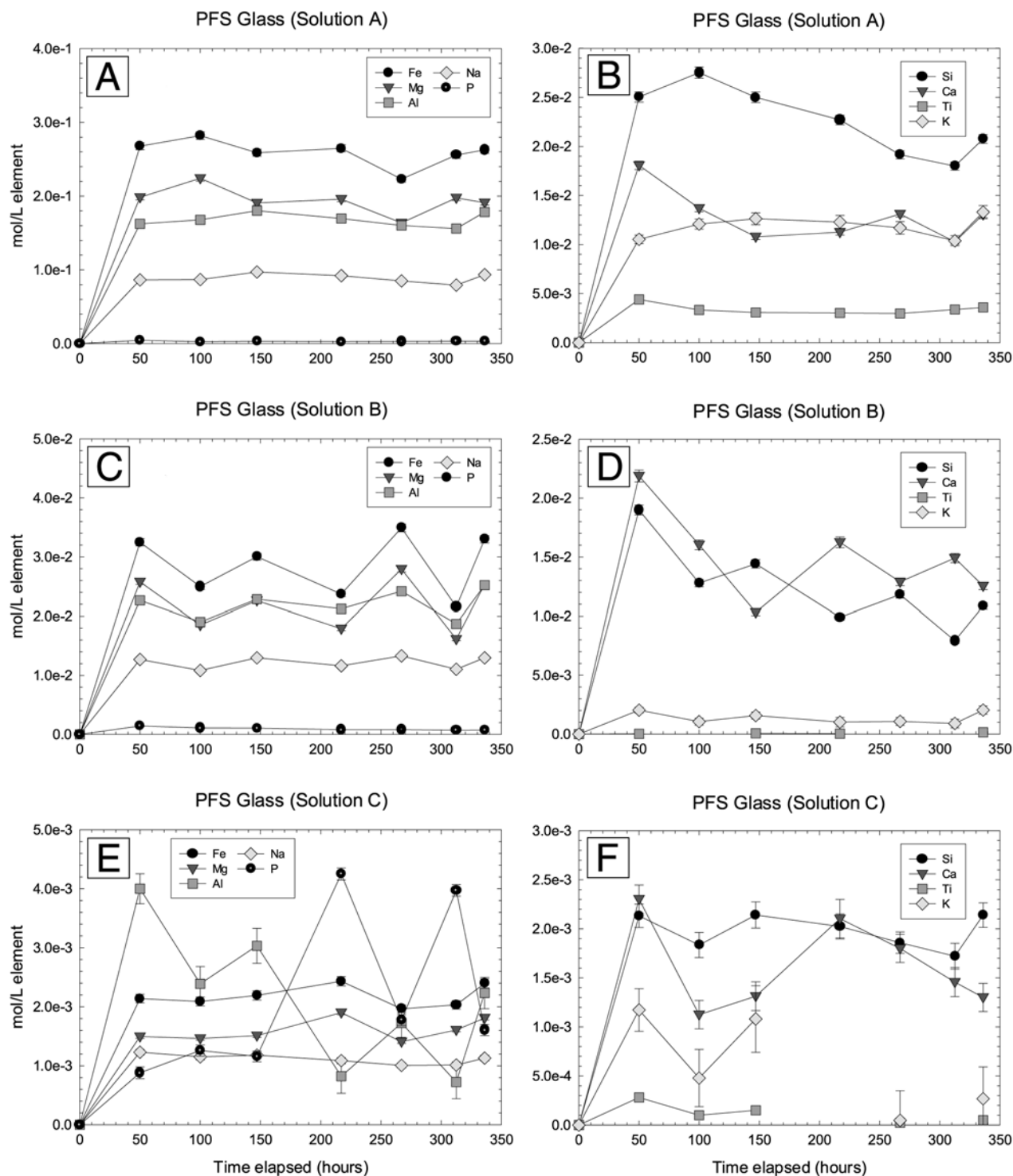


Figure A7. Major element solution concentrations during reaction with PFS glass and (a and b) solution A, (c and d) solution B, and (e and f) solution C.

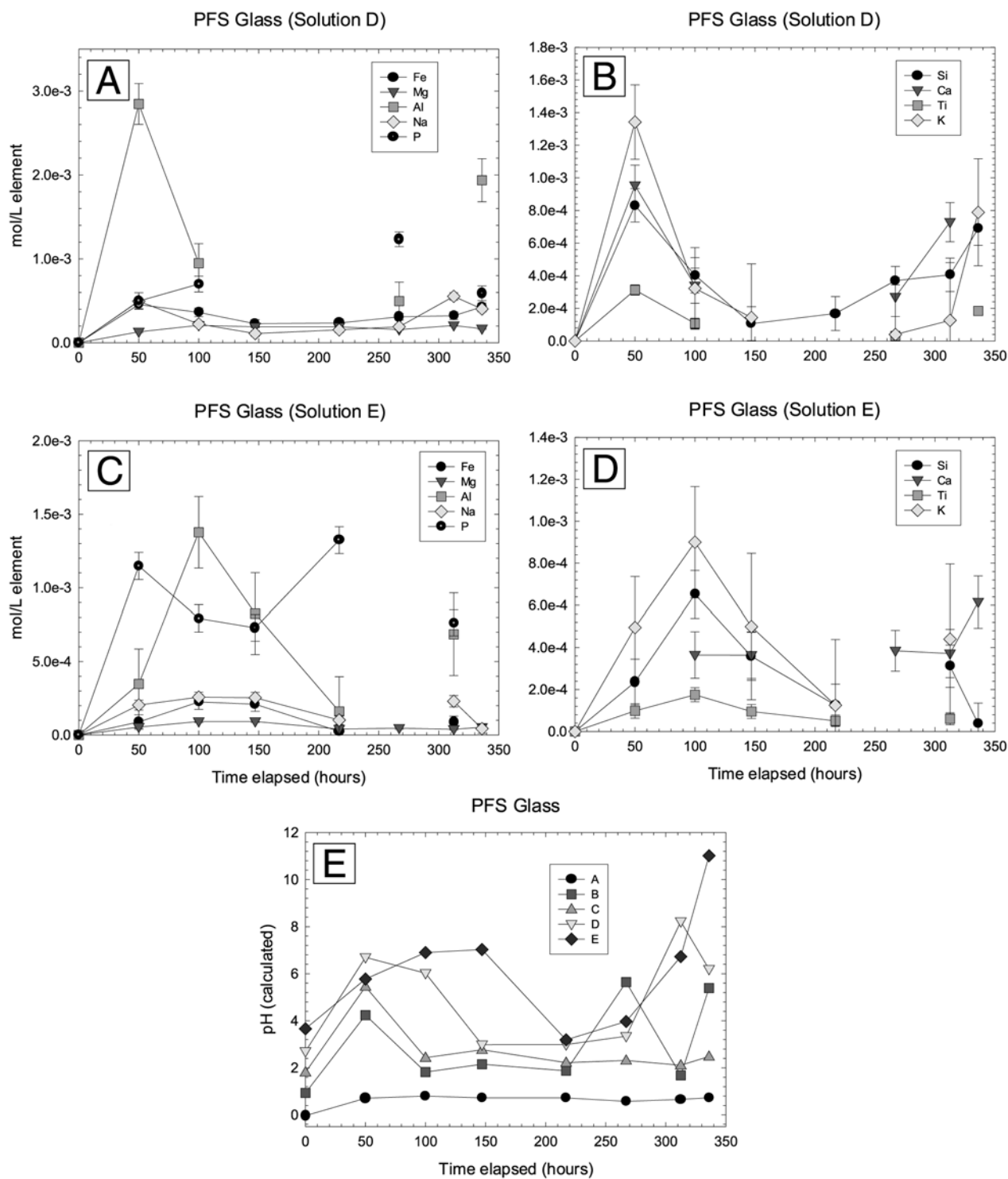


Figure A8. Major element solution concentrations during reaction with PFS glass and (a and b) solution D and (c and d) solution E. (e) Calculated pH values during reaction.

eralogy in evaluating Martian soil formation models, which may have been important throughout Martian history. Major conclusions of this work include:

[88] Acid-sulfate weathering of two relevant synthetic basaltic analogs has produced a variety of putative sulfate, Fe oxide and secondary silica alteration phases.

[89] The acid fog model requires short, intermittent basalt-fluid reactions, which limit elemental contribution to fluids to the initial stages of dissolution. In most cases, dissolution is initially nonstoichiometric resulting from ion exchange at mineral surfaces, which buffers weakly acidic solutions at a higher pH. Initial reactivity of primary Martian basalt may also be enhanced because of ongoing physical weathering.

[90] Olivine dissolution controls fluid chemistry with rapid Fe, Mg and Si release in reactions with PFS basalt. When olivine is not present (PFR basalt), pyroxenes and plagioclase dominate the solutions (with Fe-Ti oxides) by nonstoichiometric dissolution of Ca, Na and Fe, while Mg release is significantly inhibited, most likely due to stronger bonding characteristics within the pyroxene.

[91] Bulk chemical composition of basaltic glass is a significant factor in its reactivity in aqueous environments on Mars. Silica content controls glass network structure and polymerization, affecting reactivity of the bulk material. A difference of approximately 9 wt% silica has resulted in orders of magnitude differences in cation release rates to solution.

[92] The nonstoichiometric dissolution of basaltic glass has resulted in the production of residual depleted silica layers, which possess unique chemical and physical properties. In addition to this material being a source of amorphous silica on Mars, the possibility exists for clay mineral formation in these layers, if aqueous conditions permit. However, reaction times for clay nucleation are important, and the acid fog model is unlikely to account for the synthesis of well-crystallized phyllosilicates on Mars under such short reaction timescales.

Appendix A: Major Element Solution Analyses

[93] Major element solution analyses were conducted using a direct current plasma atomic emission spectrophotometer (DCP-AES). Figures A1 through A8 include solution data collected during reaction of the four mineral systems (PFR and PFS basalt/glass) with five different acid levels (solutions A–E) as well as the calculated pH values for these reactions. Figures A1 and A2 show solution and pH data for PFR basalt reactions. Figures A3 and A4 show these data for PFS basalt reactions. Figures A5 and A6 show PFR glass reactions, and Figures A7 and A8 show PFS glass reactions.

[94] **Acknowledgments.** This work was supported by NASA Cosmochemistry Program grants NAG5-10506 and NAG5-12916 to S.M.M. The authors would like to thank James Quinn for assistance with SEM analyses, John Parise and Aaron Celestian for the use of, and assistance with, XRD facilities, and Joel Hurowitz for thoughtful reviews and helpful discussions. The authors also thank Leslie Baker and an anonymous reviewer, whose comments greatly improved the quality of this manuscript.

References

- Allen, C. C., J. L. Gooding, M. J. Jercinovic, and K. Keil (1981), Altered basaltic glass: A terrestrial analog to the soil of Mars, *Icarus*, **45**, 347–369.

- Andersen, D. J., D. H. Lindsley, and P. M. Davidson (1993), QUILF: A PASCAL program to assess equilibria among Fe-Mg-Mn-Ti oxides, pyroxenes, olivine and quartz, *Comput. Geosci.*, **19**, 1333–1350.
- Baker, L. L., D. J. Agenbroad, and S. A. Wood (2000), Experimental hydrothermal alteration of a Martian analog basalt: Implications for Martian meteorites, *Meteorit. Planet. Sci.*, **35**, 31–38.
- Bandfield, J. L. (2002), Global mineral distributions on Mars, *J. Geophys. Res.*, **107**(E6), 5042, doi:10.1029/2001JE001510.
- Bandfield, J. L., V. E. Hamilton, and P. R. Christensen (2000), A global view of Martian surface compositions from MGS-TES, *Science*, **287**, 1626–1630.
- Banin, A. (1996), The missing crystalline minerals in Mars soil, *Adv. Space Res.*, **18**, 233–240.
- Banin, A., and L. Margulies (1983), Simulation of Viking biology experiments suggests smectites not palagonite, as Martian soil analogues, *Nature*, **305**, 523–525.
- Banin, A., B. C. Clark, and H. Wanke (1992), Surface chemistry and mineralogy, in *Mars*, edited by H. H. Kieffer et al., pp. 594–625, Univ. of Ariz. Press, Tucson.
- Banin, A., F. X. Han, I. Kan, and A. Cicelsky (1997), Acidic volatiles and the Mars soil, *J. Geophys. Res.*, **102**, 13,341–13,356.
- Bell, J. F. (1996), Iron, sulfate, carbonate, and hydrated minerals on Mars, in *Mineral Spectroscopy: A Tribute to Roger G. Burns*, edited by M. D. Dyar, C. McCammon, and M. W. Schaefer, *Spec. Publ. Geochem. Soc.*, **5**, 359–380.
- Bell, J. F., T. B. McCord, and P. D. Owensby (1990), Observational evidence of crystalline iron oxides on Mars, *J. Geophys. Res.*, **95**, 14,447–14,461.
- Bell, J. F., et al. (2000), Mineralogic and compositional properties of Martian soil and dust: Results from Mars Pathfinder, *J. Geophys. Res.*, **105**, 1721–1755.
- Bethke, C. M. (2002), *The Geochemist's Workbench, Release 4.0: A User's Guide to Rxn, Act2, Tact, React and Gplot*, Univ. of Ill., Urbana-Champaign.
- Bigham, J. M., and D. K. Nordstrom (2000), Iron and aluminum hydroxysulfates from acid sulfate waters, in *Sulfate Minerals: Crystallography, Geochemistry and Environmental Significance*, edited by C. N. Alpers, J. L. Jambor, and D. K. Nordstrom, pp. 351–403, Mineral. Soc. of Am., Washington, D. C.
- Bish, D. L., D. T. Vaniman, C. Fialips, J. W. Carey, and W. C. Feldman (2003), Can hydrous minerals account for the observed mid-latitude water on Mars?, paper presented at Sixth International Mars Conference, Lunar and Planet. Inst., Pasadena, Calif.
- Bishop, J. L., and E. Murad (1996), Schwertmannite on Mars? Spectroscopic analyses of schwertmannite, its relationship to other ferric minerals, and its possible presence in the surface material on Mars, in *Mineral Spectroscopy: A Tribute to Roger G. Burns*, edited by M. D. Dyar, C. McCammon, and M. W. Schaefer, *Spec. Publ. Geochem. Soc.*, **5**, 337–358.
- Bishop, J. L., C. M. Pieters, and R. G. Burns (1993), Reflectance and Mossbauer spectroscopy of ferrihydrite-montmorillonite assemblages as Mars soil analog materials, *Geochim. Cosmochim. Acta*, **57**, 4583–4595.
- Blum, A. E., and L. L. Stillings (1995), Feldspar dissolution kinetics, in *Chemical Weathering Rates of Silicate Minerals*, edited by A. F. White and S. L. Brantley, pp. 291–351, Mineral. Soc. of Am., Washington, D. C.
- Bouska, V. (1993), *Natural Glasses*, Ellis Horwood, New York.
- Brantley, S. L., and Y. Chen (1993), Chemical weathering rates of pyroxenes and amphiboles, in *Chemical Weathering Rates of Silicate Minerals*, edited by A. F. White and S. L. Brantley, pp. 119–172, Mineral. Soc. of Am., Washington, D. C.
- Bridges, J. C., and M. M. Grady (1999), A halite-siderite-anhydrite-chlorapatite assemblage in Nakhla: Mineralogical evidence for evaporites on Mars, *Meteorit. Planet. Sci.*, **34**, 407–415.
- Bridges, J. C., D. C. Catling, J. M. Saxton, T. D. Swindle, I. C. Lyon, and M. M. Grady (2001), Alteration assemblages in Martian meteorites: Implications for near-surface processes, *Space Sci. Rev.*, **96**, 365–392.
- Casey, W. H., and B. Bunker (1990), Leaching of mineral and glass surfaces during dissolution, in *Mineral-Water Interface Geochemistry*, edited by A. F. White and M. F. Hochella, pp. 397–426, Mineral. Soc. of Am., Washington D. C.
- Casey, W. H., H. R. Westrich, and G. W. Arnold (1988), Surface chemistry of labradorite feldspar reacted with aqueous solutions at pH = 2, 3, and 12, *Geochim. Cosmochim. Acta*, **52**, 2795–2807.
- Casey, W. H., J. F. Banfield, H. R. Westrich, and L. McLaughlin (1993), What do dissolution experiments tell us about natural weathering?, *Chem. Geol.*, **105**, 1–15.
- Christensen, P. R., et al. (2000), Detection of crystalline hematite mineralization on Mars by the Thermal Emission Spectrometer: Evidence for near-surface water, *J. Geophys. Res.*, **105**, 9623–9642.

- Clark, B. C. (1993), Geochemical components in Martian soil, *Geochim. Cosmochim. Acta*, 57, 4575–4581.
- Clark, B. C., and D. C. Van Hart (1981), The salts of Mars, *Icarus*, 45, 370–378.
- Economou, T. E. (2001), Chemical analyses of Martian soil and rocks obtained by the Pathfinder alpha proton x-ray spectrometer, *Radiat. Phys. Chem.*, 61, 191–197.
- Eggleson, C. M., M. F. Hochella, and G. A. Parks (1989), Sample preparation and aging effects on the dissolution rate and surface composition of diopside, *Geochim. Cosmochim. Acta*, 53, 797–805.
- Foley, C. N., T. Economou, and R. N. Clayton (2003), Final chemical results from the Mars Pathfinder alpha proton X-ray spectrometer, *J. Geophys. Res.*, 108(E12), 8096, doi:10.1029/2002JE002019.
- Ghiorso, M. S., and R. O. Sack (1995), Chemical mass transfer in magmatic processes. IV. A revised and internally consistent thermodynamic model for the interpolation and extrapolation of liquid-solid equilibria in systems at elevated temperatures and pressures, *Contrib. Mineral. Petrol.*, 119, 197–212.
- Gibson, E. K., D. S. McKay, S. J. Wentworth, and R. A. Socki (2003), Zeolite formation and weathering processes within the Martian regolith: An Antarctic analog, *Lunar Planet. Sci.*, XXXIV, abstract 1244.
- Glass, B. P. (1984), Solution of naturally occurring glasses in the geological environment, *J. Non Cryst. Solids*, 67, 265–286.
- Golden, D. C., R. V. Morris, D. W. Ming, H. V. Lauer, and S. R. Yang (1993), Mineralogy of three slightly palagonitized basaltic tephra samples from the summit of Mauna Kea, Hawaii, *J. Geophys. Res.*, 98, 3401–3411.
- Gooding, J. L. (1992), Soil mineralogy on Mars: Possible clues from salts and clays in SNC meteorites, *Icarus*, 99, 28–41.
- Gooding, J. L., and K. Keil (1978), Alteration of glass as a possible source of clay minerals on Mars, *Geophys. Res. Lett.*, 5, 727–730.
- Herd, C. D. K., J. J. Papike, and A. J. Brearley (2001), Oxygen fugacity of Martian basalts from electron microprobe oxygen and TEM-EELS analyses of Fe-Ti oxides, *Am. Mineral.*, 86, 1015–1024.
- Hoefen, T. M., R. N. Clark, J. L. Bandfield, M. D. Smith, J. C. Pearl, and P. R. Christensen (2003), Discovery of olivine in the Nili Fossae region of Mars, *Science*, 302, 627–630.
- Holdren, G. R., and R. A. Berner (1979), Mechanism of feldspar weathering. I. Experimental studies, *Geochim. Cosmochim. Acta*, 43, 1161–1171.
- Jambor, J. L., D. K. Nordstrom, and C. N. Alpers (2000), Metal-sulfate salts from sulfide mineral oxidation, in *Sulfate Minerals: Crystallography, Geochemistry and Environmental Significance*, edited by C. N. Alpers, J. L. Jambor, and D. K. Nordstrom, pp. 305–350, Mineral. Soc. of Am., Washington, D. C.
- Jantzen, C. M., and M. J. Plodinec (1984), Thermodynamic model of natural, medieval and nuclear waste glass durability, *J. Non Cryst. Solids*, 67, 207–223.
- Knauss, K. G., S. N. Nguyen, and H. C. Weed (1993), Diopside dissolution kinetics as a function of pH, CO₂, temperature, and time, *Geochim. Cosmochim. Acta*, 57, 285–294.
- Lasaga, A. C. (1998), *Kinetic Theory in the Earth Sciences*, Princeton Univ. Press, Princeton, N. J.
- McLennan, S. M. (2000), Chemical composition of Martian soil and rocks: Complex mixing and sedimentary transport, *Geophys. Res. Lett.*, 27, 1335–1338.
- McLennan, S. M. (2001), Crustal heat production and the thermal evolution of Mars, *Geophys. Res. Lett.*, 28, 4019–4022.
- McLennan, S. M. (2003), Sedimentary silica on Mars, *Geology*, 31, 315–318.
- McSween, H. Y., and K. Keil (2000), Mixing relationships in the Martian regolith and the composition of globally homogeneous dust, *Geochim. Cosmochim. Acta*, 64, 2155–2166.
- McSween, H. Y., et al. (1999), Chemical, multispectral and textural constraints on the composition and origin of rocks at the Mars Pathfinder landing site, *J. Geophys. Res.*, 104, 8679–8715.
- Minitti, M. E., and M. J. Rutherford (1999), Genesis of the Mars Pathfinder sulfur-free rock from a SNC parental magma, *Lunar Planet. Sci.*, XXX, abstract 1198.
- Morris, R. V., J. L. Gooding, H. V. Lauer, and R. B. Singer (1990), Origins of Marslike spectral and magnetic properties of a Hawaiian palagonitic soil, *J. Geophys. Res.*, 95, 14,427–14,434.
- Morris, R. V., D. W. Ming, D. C. Golden, and J. F. Bell (1996), An occurrence of jarositic tephra on Mauna Kea, Hawaii: Implications for the ferric mineralogy of the Martian surface, in *Mineral Spectroscopy: A Tribute to Roger G. Burns*, edited by M. D. Dyar, C. McCammon, and M. W. Schaefer, *Spec. Publ. Geochem. Soc.*, 5, 327–336.
- Morris, R. V., et al. (2000a), Mineralogy, composition and alteration of Mars Pathfinder rocks and soils: Evidence from multispectral, elemental and magnetic data on terrestrial analogue, SNC meteorite and Pathfinder samples, *J. Geophys. Res.*, 105, 1757–1817.
- Morris, R. V., et al. (2000b), Acid sulfate alteration products of a tholeiitic basalt: Implications for interpretation of Martian thermal emission spectra, *Lunar Planet. Sci.*, XXXI, abstract 2014.
- Morris, R. V., T. G. Graff, S. A. Mertzman, M. D. Lane, and P. R. Christensen (2003), Palagonitic Mars from rock rinds to dust: Evidence from visible, near-IR, and thermal emission spectra of poorly crystalline materials, *Lunar Planet. Sci.*, XXXIV, abstract 1874.
- Morse, J. W., and G. M. Marion (1999), The role of carbonates in the evolution of early Martian oceans, *Am. J. Sci.*, 299, 738–761.
- Mustard, J. F., and J. M. Sunshine (1995), Seeing through the dust: Martian crustal heterogeneity and links to the SNC meteorites, *Science*, 267, 1623–1626.
- Mustard, J. F., S. Erard, J.-P. Bibring, J. W. Head, S. Hurtrez, Y. Langevin, C. M. Pieters, and C. J. Sotin (1993), The surface of Syrtis Major: Composition of the volcanic substrate and mixing with altered dust and soil, *J. Geophys. Res.*, 98, 3387–3400.
- Oelkers, E. H. (2001), General kinetic description of multioxide silicate mineral and glass dissolution, *Geochim. Cosmochim. Acta*, 65, 3703–3719.
- Oelkers, E. H., and S. R. Gislason (2001), The mechanism, rates and consequences of basaltic glass dissolution: I. An experimental study of the dissolution rates of basaltic glass as a function of aqueous Al, Si and oxalic acid concentration at 25°C and pH = 3 and 11, *Geochim. Cosmochim. Acta*, 65, 3671–3681.
- Petrovich, R. (1981), Kinetics of dissolution of mechanically comminuted rock-forming oxides and silicates, II. Deformation and dissolution of oxides and silicates in the laboratory and at the Earth's surface, *Geochim. Cosmochim. Acta*, 45, 1675–1686.
- Poraj-Kosic, E. A. (1977), The structure of glass, *J. Non Cryst. Solids*, 25, 87–128.
- Ptacek, C., and D. Blowes (2000), Predicting sulfate-mineral solubility in concentrated waters, in *Sulfate Minerals: Crystallography, Geochemistry and Environmental Significance*, edited by C. N. Alpers, J. L. Jambor, and D. K. Nordstrom, pp. 513–540, Mineral. Soc. of Am., Washington, D. C.
- Rieder, R., T. E. Economou, H. Wanke, A. Turkevich, J. Crisp, J. Bruckner, G. Dreibus, and H. Y. McSween Jr. (1997), The chemical composition of Martian soil and rocks returned by the mobile alpha proton x-ray spectrometer: Preliminary results from the x-ray mode, *Science*, 278, 1771–1774.
- Schott, J., and R. A. Berner (1983), X-ray photoelectron studies of the mechanism of iron silicate dissolution during weathering, *Geochim. Cosmochim. Acta*, 47, 2233–2240.
- Schott, J., and R. A. Berner (1985), Dissolution mechanisms of pyroxenes and olivines during weathering, in *The Chemistry of Weathering*, edited by J. I. Drever, pp. 35–54, Kluwer Acad., Norwell, Mass.
- Settle, M. (1979), Formation and deposition of volcanic sulfate aerosols on Mars, *J. Geophys. Res.*, 84, 8343–8354.
- Singer, R. B., T. B. McCord, R. N. Clark, J. B. Adams, and R. L. Huguening (1979), Mars surface composition from reflectance spectroscopy: A summary, *J. Geophys. Res.*, 84, 8415–8426.
- Soderblom, L. A. (1992), The composition and mineralogy of the Martian surface from spectroscopic observations: 3 μ m to 50 μ m., in *Mars*, edited by H. H. Kieffer et al., pp. 557–593, Univ. of Ariz. Press, Tucson.
- Stillings, L. L., and S. L. Brantley (1995), Feldspar dissolution at 25°C and pH 3: Reaction stoichiometry and the effect of cations, *Geochim. Cosmochim. Acta*, 59, 1483–1496.
- Stumm, W., and J. J. Morgan (1996), *Aquatic Chemistry: An Introduction Emphasizing Chemical Equilibria in Natural Waters*, John Wiley, New York.
- Toulmin, P., A. K. Baird, B. C. Clark, K. Keil, H. J. Rose, R. P. Christian, H. P. Evans, and W. C. Kelliher (1977), Geochemical and mineralogical interpretation of the Viking inorganic chemical results, *J. Geophys. Res.*, 82, 4625–4634.
- Wänke, H., J. Bruckner, G. Dreibus, R. Rieder, and I. Ryabchikov (2001), Chemical composition of rocks at the Pathfinder site, *Space Sci. Rev.*, 96, 317–330.
- White, A. F. (1990), Heterogeneous electrochemical reactions associated with oxidation of ferrous oxide and silicate surfaces, in *Mineral-Water Interface Geochemistry*, edited by A. F. White and M. F. Hochella, pp. 467–509, Mineral. Soc. of Am., Washington, D. C.
- Wyatt, M. B., and H. Y. McSween (2002), Spectral evidence for weathered basalt as an alternative to andesite in the northern lowlands of Mars, *Nature*, 417, 263–266.

D. H. Lindsley, S. M. McLennan, M. A. A. Schoonen, and N. J. Tosca,
Department of Geosciences, State University of New York, Stony Brook,
NY 11794-2100, USA. (ntosca@ic.sunysb.edu)